DEPARTMENT OF THEORETICAL PHYSICS AND COMPUTER MODELLING

Head of Department *Dr. hab. phys*. Eugene Kotomin

Research Area and Main Problems

Our theoretical research interests are focused on six classes of problems related to:

- kinetics of diffusion-controlled processes, with emphasis on pattern formation and catalytic surface reactions;
- the atomic and electronic structure of numerous 3D and 2D advanced materials, with emphasis on calculations of properties of defects, surfaces, metal/insulator interfaces;
- theoretical simulations and experimental studies of 1D and 0D advanced nanomaterials, *e.g.*, evaluation of their photocatalytic suitability;
- modeling of advanced functional materials for energy applications (fuel cells, ceramic membranes, fusion and fission reactors);
- gyrotron development for thermonuclear reactors

We combine several different techniques, including analytical formalisms and large-scale computer simulations (quantum chemical methods, stochastic simulations as well as Monte Carlo/cellular automata modeling) as described in our homepage http://www1.cfi.lu.lv/teor

Staff

Laboratory of kinetics in self-organizing systems	Laboratory of computer modeling of electronic structure of solids
Dr. O. Dumbrajs (full member of Latvian Acad. Sci.)	Dr. D. Bocharov
Dr. D. Gryaznov	Dr. R. Eglitis (corr. member of Latvian Acad. Sci.)
Dr. E. Klotins	Dr. Yu. Mastrikov
Dr. hab. E. Kotomin (full member of Latvian Acad. Sci.)	Dr. S. Piskunov
Dr. hab. V. Kuzovkov	Dr. hab. Yu. Shunin
Dr. A. Popov	Dr. Yu. Zhukovskii
Dr. G. Zvejnieks	M.S. A. Gopejenko
M.S. A. Chesnokov	M.S. O. Lisovski
M.S. J. Shirmane (Pankratova)	M.S. A. Platonenko
B.S. A. Moskina	B.S. M. Sokolov

Scientific visits abroad

1. Dr. hab. E. Kotomin, Max-Planck Institut für Festkörperforschung, Stuttgart, Germany (6 months), Photochemistry Center, Russian Academy of Sciences, Moscow (1 week)
2. Dr. O. Dumbrajs, University of Fukui, Japan (3 months)
3. Dr. D. Gryaznov, Max-Planck Institut für Festkörperforschung, Stuttgart, Germany (1 week).
4. Dr. A. Popov, Max-Planck Institut für Festkörperforschung, Stuttgart, Germany (1.5 weeks), Institute of Physics, University of Tartu, Estonia (1.5 weeks)
5. Dr. Yu. Mastrikov, Institut für Angewandte Materialien, Karlsruhe Institut für Technologie, Germany (2 weeks).
6. Dr. S. Piskunov, Institute of General and Inorganic Chemistry, Russian Academy of Sciences, Moscow (2.5 months); University of Duisburg-Essen, Germany (2 weeks).
7. Dr. hab. Yu. Shunin, Laboratori Nazionali di Frascati, Italy (1 month).
8. Dr. Yu. Zhukovskii, St. Petersburg State University, Russia (2 weeks); Institute of General and Inorganic Chemistry, Russian Academy of Sciences, Moscow (1 week).
9. M.S. O. Lisovski, University of Duisburg-Essen, Germany (6.5 months).

International Cooperation

China	1. Beijing Institute of Technology, Beijing (Dr. H. Shi).
Estonia	2. Institute of Physics, University of Tartu (Prof. A. Lushchik)
Finland	3. Helsinki University of Technology, Espoo (Dr. T. Kurki-Suonio)
France	4. Laue-Langevin Institute, Grenoble, Prof. H. Schober)
Germany	5. Max Planck Institut für Festkörperforschung, Stuttgart (Prof. Dr. J. Maier) 6. Deutsches Elektronen-Synchrotron DESY, Hamburg (Dr. A. Kotlov) 7. Darmstadt University of Technology, Darmstadt (Prof. H. von Seggern) 8. Institut für Hochleistungsimpuls & Mikrowellentechnik (KIT), Karlsruhe (Dr. S. Kern, Dr. B. Piosczyk) 9. Max-Planck Institut für Plasmaphysik, Garching, (Prof. Dr. H. Zohm) 10. Institut für Angewandte Materialien (KIT), Karlsruhe (Prof. Dr. A. Möslang, Dr. P. Vladimirov) 11. Dept Theoretical Chemistry, Univ. Duisburg-Essen (Prof. Dr. E. Spohr)
Israel	12. Ben Gurion University, Beer Sheva (Prof. D. Fuks)
Italy	13. Laboratori Nazionali di Frascati (Dr. S. Bellucci, Dr. M. Cestelli-Guidi)
Kazakhstan	14. Gumilyov Eurasian National University, Astana (Prof. A.T. Akilbekov)
Japan	15. FIR Center, University of Fukui (Prof. T. Idehara)
Lithuania	16. Institute of Semiconductor Physics (SPI), Vilnius (Dr. E. Tornau)
Norway	17. Center for Materials Science and Nanotechnology, Department of Chemistry, University of Oslo, FASE, Norway (Dr. T. Bjørheim)
Poland	18. Warsaw University, Department of Chemistry (Prof. A. Huczko, Prof. Dąbrowska) 19. Institute of Physics, Academy of Science, Warsaw (Prof. H. Szymczak)
Romania	20. University of Craiova (Dr. D. Constantinescu)

Russia	21. St. Petersburg State University, Petrodvorets (St. Petersburg) (Prof. R. A. Evarestov) 22. Institute of General and Inorganic Chemistry, Russian Academy of Sciences, Moscow (Prof. P.N. D'yachkov) 23. Photochemistry Center, Russian Academy of Sciences, Moscow (Prof. A.A. Bagaturyants)
Spain	24. Centro de Investigaciones Energeticas Medioambientales y Tecnologicas (CIEMAT), Madrid (Dr. R. Vila)
UK	25. University College London (Prof. A.L. Shluger)
Ukraine	26. Ivan Franko National University, Lviv (Prof. O. I. Aksimentyeva, Prof. I. Bolesta, Dr. I. Karbovnyk)
USA	27. University of Maryland, College Park (Dr. G.S. Nusinovich, Dr. M.M. Kukla)

Main Results

A. Electronic structure calculations for advanced materials

First principles computer modeling of complex perovskites for fuel cell and permeation membrane applications

Yu.A. Mastrikov, E.A. Kotomin

L.F. Liotta,

Institute for the Study of Nanostructured Materials (ISMS)-CNR, University of Palermo, Italy

Environmentally friendly solid oxide fuel cells operated at intermediate temperatures, 800-1000 K (IT-SOFC), are internsively investigated due to their potential high efficiency in energy conversion. Currently, the two most promising cathode materials for cathodes and permeation membranes are (Ba,Sr)(Co,Fe)O_3 (BSCF) and (La,Sr)(Co,Fe)O_3 (LSCF).

Comparing these materials, BSCF shows better performance but has several shortcomings, including irreversible transformation into hexagonal phase and carbonate formation in CO_2-containing atmosphere. In turn, LSCF is more stable and thus, being further doped with metal on *B*-sublattice, could serve as a promising candidate for IT-SOFC cathode. (La,Sr)(Co,Fe)O_3 (LSCF) perovskites are well known promising materials for cathodes of solid oxide fuel cells. In order to reduce cathode operational temperature, doping on *B*-sublattice metals was suggested.

Indeed, as it was experimentally shown recently, doping with low Pd content increases oxygen vacancy concentration which is one of factors controlling oxygen transport in fuel cells.

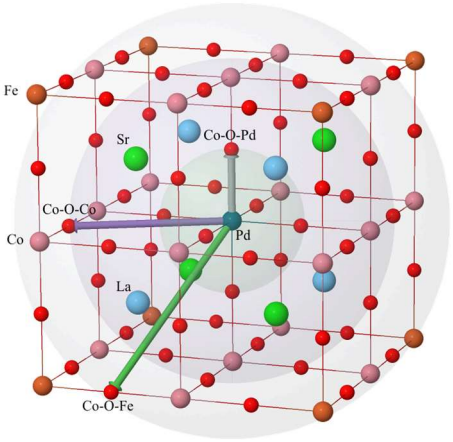

Figure 1. Model of $La_{0.5}Sr_{0.5}Co_{0.5}Fe_{0.25}Pd_{0.25}O_3$ supercell. Three nonequivalent types of oxygen positions are indicated: Co-O-Pd (25%), Co-O-Co (50%), Co-O-Fe (25%).

In this study, we modeled this material using fist principles DFT calculations combined with a supercell model. The charge density redistribution, density of states, and local lattice distortion around Pd ions are analyzed and reduction of the vacancy formation energy confirmed.

Ab initio calculations of surface segregation entropy of oxygen vacancies and protons in $BaZrO_3$ crystals and thin films

E.A. Kotomin,

M. Arrigoni, J. Maier,

Max Planck Institute for Solid State Research, Stuttgart, Germany

T.S. Bjørheim

Centre for Materials Science and Nanotechnology, Department of Chemistry, University of Oslo, Norway

The perovskite $BaZrO_3$ has attracted considerable attention in the recent decade due to its high temperature proton conducting properties, and possible application as electrolyte in intermediate temperature fuel cells and electrolyzers. We performed, for the first time, ab initio calculations of the phonon contribution to the defect thermodynamics of the ZrO_2 terminated (001) surface of $BaZrO_3$. The approach allows us to determine both the *segregation enthalpy* and *entropy* of defects, appled for two fundamental *d*-vacancies (effects in $BaZrO_3$: fully charged oxygen $v_O^{\bullet\bullet}$ and protonic $OH_O^{\bullet}$ defects).

The calculations show that both defects exhibit favorable segregation enthalpies of -65 and -125 kJ/mol, respectively. Further, the vibrational formation entropy of the surface $v_O^{\bullet\bullet}$ vacancy is significantly higher than that of bulk $v_O^{\bullet\bullet}$ vacancy, due to smaller local structural relaxations of the surface defect, leading to a finite surface segregation entropy of 53 J/molK. $OH_O^{\bullet}$, on the other hand, displays nearly identical vibrational spectra at the surface and in the bulk, and the segregation entropy is therefore negligible.

Hence, phonons not only stabilize the surface $v_O^{\bullet\bullet}$ vacancies compared to the bulk defect thermodynamically at high temperatures, but also affect the relative stability of $v_O^{\bullet\bullet}$ and $OH_O^{\bullet}$ at the surface. Finally, we applied a simplified space charge model to the (001) surface, and show that neglect of phonons results in underestimated surface concentration of $v_O^{\bullet\bullet}$ vacancies.

We studied also possible confinement effects on the atomic and electronic structure, and phonon properties of neutral ($v_O^{\times}$) and fully charged ($v_O^{\bullet\bullet}$) oxygen vacancies in $BaZrO_3$ (001) ultra-thin films.

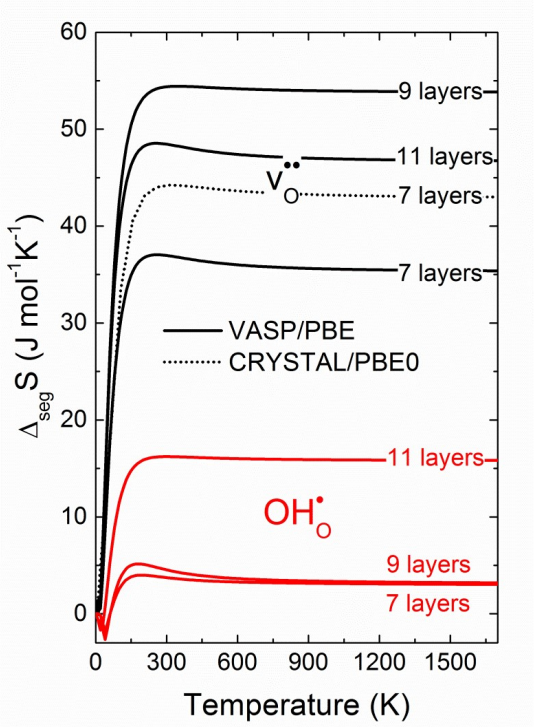

Figure 2. The vibrational contribution to the Gibbs free energy of $v_O^{\bullet\bullet}$ and $OH_O^{\bullet}$ calculated with 7, 9 and 11 atomic layer thick slabs of the ZrO_2 terminated (001) surface of $BaZrO_3$. For $v_O^{\bullet\bullet}$ vacancies, the calculations were performed with both VASP/PBE (solid black) and CRYSTAL/PBE0 computer codes (dotted black) for comparison.

First principles phonon calculations were performed also as a function of film thickness (from 3- to 7-atomic planes) using two complementary DFT methods. The calculations reveal that for both types of vacancies, the confinement effect is very short-range; for films containing 5 planes or more, the $v_O^{\bullet\bullet}$ vacancy properties are predicted to be similar to those observed in the bulk material.

Hybrid Density Functional Theory – Hartree-Fock calculations of oxygen vacancies and protons in complex perovskite oxides

D. Gryaznov, E.A. Kotomin

M. Arrigoni, J. Maier

Max Planck Institute for Solid State Research, Heisenbergstrasse 1, Stuttgart, Germany

Among fuel cells with ceramic electrolytes, those based on proton-conducting oxides (protonic ceramic fuel cells, PCFC) attract increasing interest. In particular, proton-conducting ceramic electrolytes, such as acceptor-doped $BaZrO_3$ discussed above, offer a higher ionic conductivity compared to standard zirconia or ceria oxygen ion conductors, in particular in the temperature range below 700 °C.

The main limiting factors in such cells are (*i*) the manufacturing of a thin electrolyte membrane with non-blocking grain boundaries, and (*ii*) optimization of cathode materials for application on a proton-conducting electrolyte. For cathodes on oxygen ion conducting electrolytes it has been shown that - in addition to a sufficient electronic conductivity - the cathode should be also conducting for oxygen ions to allow the oxygen reduction reaction to extend beyond the gas/cathode/electrolyte three-phase boundary.

Analogously, for PCFC the cathode should exhibit a certain proton concentration and corresponding proton conductivity. However, a proton conductivity in the range of 10^{-5} S/cm at operation conditions (*i.e.* much lower than that of the electrolyte) was estimated to suffice for this purpose.

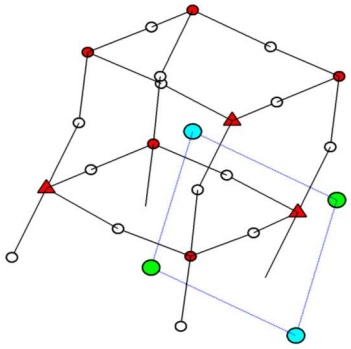

Figure 3. The schematic three-dimensional section of $La_{0.5}Sr_{0.5}FeO_3$ structure; O = white circles, Fe = red, La = green, Sr = cyan. Fe ions in 4^+ oxidation state are indicated by triangles

Using hybrid density functionals, detailed *ab initio* calculations based on the linear combination of atomic orbitals (LCAO) formalism were performed for $v_O^{\bullet\bullet}$ vacancies and protons in $La_{1-x}Sr_xFeO_{3-\delta}$ perovskites serving as cathode material in PCFC. The atomic and electronic structure of different defect configurations and the role of Fe oxidation state are analyzed in detail. The energetics of the reduction and hydration reactions was stadied. The hydration energy is found to be markedly smaller than in the case of $Ba(Zr_{1-x}Y_x)O_3$, and the role of material's *basicity* is discussed as a decisive factor.

First principles calculations of *F* centers in $SrZrO_3$ perovskite bulk and ZrO_2-terminated (001) surface.

R.I. Eglitis, S. Piskunov

Using a supercell model and B3PW hybrid exchange-correlation functional in the framework of the density functional theory (DFT), as implemented in the CRYSTAL computer code, we performed *ab initio* calculations for *F* center located in the $SrZrO_3$ bulk and on the ZrO_2-terminated (001) surface.

According to results of performed relaxation of atoms around the defect, the two nearest Zr and four Sr atoms are repulsed, but all O atoms are attracted towards both bulk and (001) surface *F*-center. Displacements of atoms surrounding the bulk *F* center are found to be smaller than those around the (001) surface *F*-center while the

ZrO_2-terminated (001) surface optical band gap (4.63 eV) is smaller than this value in the bulk (5.60 eV).

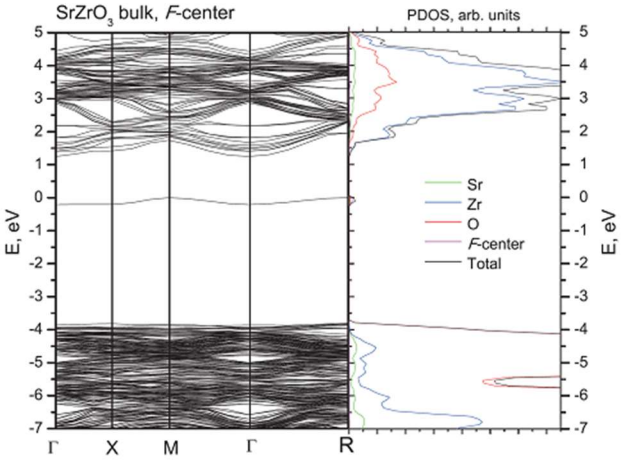

Figure 4. B3PW-calculated band structure for the $SrZrO_3$ bulk containing the isolated *F*-center (left plot) as well as total and projected DOS (right plot).

The *F* center bands for bulk and (001) surface in $SrZrO_3$ calculated using 3×3×3 and 3×3×1 supercells are located 1.12 and 0.93 eV under the conduction band bottom, respectively. The O vacancy in the $SrZrO_3$ bulk attracts 1.25*e*, and even less, only 1.10 *e* on the ZrO_2-terminated (001) surface. Performed calculations reveal significant enhancement of the chemical bond covalency among the $SrZrO_3$ bulk *F* center and its nearest Zr atoms of 0.24 *e* in comparison with the ideal $SrZrO_3$ perovskite Zr-O chemical bond covalency of 0.10 *e*. Observed defect formation energy for the *F*-center located on the ZrO_2-terminated (001) surface 7.52 eV is somewhat smaller than in the $SrZrO_3$ bulk 7.55 eV. Difference of these formation energies may trigger the segregation of the *F*-center from the $SrZrO_3$ bulk towards the ZrO_2-terminated (001) surface.

Ab initio modeling of $PbBO_3/SrBO_3$(001) heterostructures (B = Ti, Zr)

R.I. Eglitis, S. Piskunov, Yu.F. Zhukovskii

We performed *ab initio* calculations for both $PbTiO_3/SrTiO_3$(001) and $PbZrO_3/SrZrO_3$(001) heterostructures. For PbO and TiO_2-terminated $PbTiO_3$ (001) thin films of different thickness, augmented on the $SrTiO_3$ (001) substrate, the magnitudes of atomic relaxations Δz increase

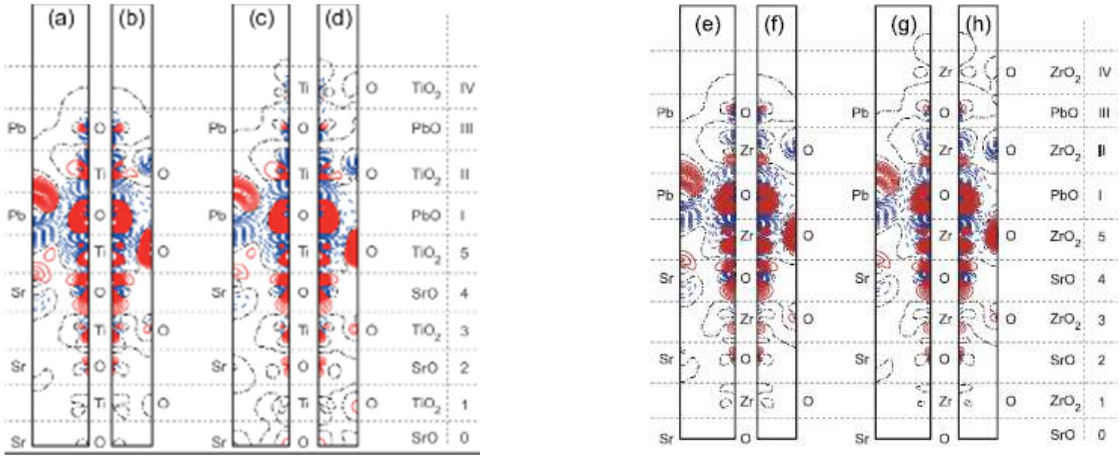

Figure 5. Difference electron charge density maps calculated for $PtTiO_3/SrTiO_3$(001) and $PtZrO_3/SrZrO_3$(001) heterostructures: (a) (110) cross-section for N_{PTO}= 3, (b) (100) cross-section for N_{PTO} = 3, (c) (110) cross-section for N_{PTO} = 4, (d) (100) cross-section for N_{PTO} = 4, (e) (110) cross-section for N_{PZO} = 3, (f) (100) cross-section for N_{PZO} = 3, (g) (110) cross-section for N_{PZO} = 4, (h) (100) cross-section for N_{PZO} = 4. Red solid (dark gray), blue dashed (light gray) and black dash-dot isolines describe positive, negative and zero values of the difference charge density, respectively. Isodensity curves are drawn from -0.025 to +0.025e Å^{-3} with an increment of 0.0005*e* Å^{-3}. Right-side bars in both plots show the atomic monolayers from which atoms are originated.

as a function of the number of monolayers. For both terminations of the augmented $PbTiO_3$ (001) nanothin film, all upper, third and fifth monolayers are displaced inwards (Δz is negative), whereas all second, fourth and sixth monolayers are displaced outwards (Δz is positive). Qualitatively similar behaviour of $PbZrO_3$(001) nanothin films above strontium zirconate substrate have been observed in $PbZrO_3/SrZrO_3$(001) heterostructures.

The B3PW hybrid exchange-correlation functional, as implemented in CRYSTAL computer code, has been used for calculations of the band gaps in various $PbTiO_3/SrTiO_3$ (001) heterostructures (irrespectively on the number of augmented PTO nanolayers) which always were found to be smaller than the band gaps for the $PbTiO_3$ and $SrTiO_3$ bulk. For both terminations, their band gaps are found to be reduced (Figure 6) due to the increased number of $PbTiO_3$(001) monolayers. The band gaps of PbO-terminated augmented $PbTiO_3$(001) films are always larger than those for TiO_2-terminated $PbTiO_3$(001) nanofilms. For each monolayer of the $SrTiO_3$(001) substrate, the charge magnitudes are always more than several times larger, than for each monolayer in the augmented $PbTiO_3$ (001) thin film.

The 2D interfaces inside considered perovskite (001) heterostructures have been also checked as electrode materials potentially suitable for photocatalytic applications, *e.g.*, for visible-light-driven dissociation of water molecules in aqueous electrolytes. Their efficiency depends on relative position of the band gap edges ε_{VB} and ε_{CB} (the visible-light interval between the infrared and ultraviolet ranges of solar spectrum corresponds to band gap widths ~1.5–2.8 eV) accompanied by a proper alignment of the valence and conduction bands (ε_{VB} and ε_{CB}) as well as occupied and unoccupied induced levels (ε_{HOIL} and ε_{LUIL}) relative to both reduction (ε_{H^+/H_2}) and oxidation (ε_{O_2/H_2O}) potentials (-4.44 eV and -5.67 eV, respectively). The latter must be positioned inside the band gap between mentioned levels:

$$\varepsilon_{VB} < \varepsilon_{HOIL} < \varepsilon_{O_2/H_2O} < \varepsilon_{H^+/H_2} < \varepsilon_{LUIL} < \varepsilon_{CB},$$

in order to satisfy photocatalytic conditions.

As follows from DOS plots (Figure 6), $PbTiO_3/SrTiO_3$(001) heterostructures containing even-layer, 4 UC-thick $PbTiO_3$ (001) nanothin film can be considered as potential candidates for hydrogen production. Nevertheless, the band gap of heterostructure containing 4 UC-thick film (~3.4 eV) corresponds to ultraviolet light range, being too wide for sunlight energy conversion (15-17%). To overcome this shortcoming, such a photoelectrode must be doped, both by metal and non-metal atoms.

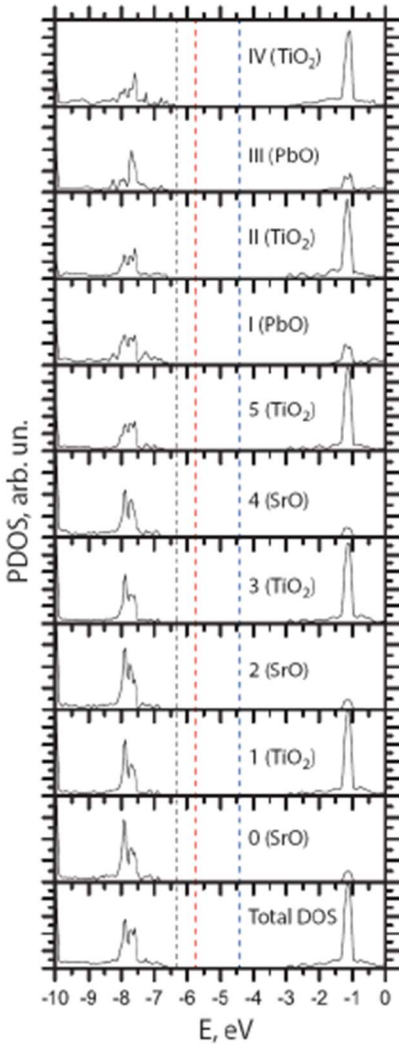

Figure 6. Layer by layer projected density of states of four unit-cell-thick $PbTiO_3/SrTiO_3$ (001) heterostructure. Energy scale is plotted regarding the vacuum level. Black vertical line corresponds to the Fermi level of heterostructure while red and blue lines describe oxidation and reduction electrochemical potentials (the latter is usually defined as the standard hydrogen potential SHE).

N- and S-doped anatase-structured TiO_2 (101) nanotubes for visible-light-driven photocatalytic water splitting: Prediction from first principles

O. Lisovski, A. Chesnokov, S. Piskunov, D. Bocharov, Yu.F. Zhukovskii

E. Spohr, M. Wessel

Department of Theoretical Chemistry, University of Duisburg-Essen, Germany

Choice of anatase-structured model for energetically stable six-layered TiO_2(101) nanotube (NT) with (-12,12) chirality (Figure 7a) is justified by a compromise between minimal formation energy and a number of atoms in the NT supercell. A nanotube of such a configuration consists of 144 atoms per unit cell (or 432 sites for Ti atoms). Four possible N or S monodopant sites are shown for non-equivalent oxygen atoms (Figure 7b).

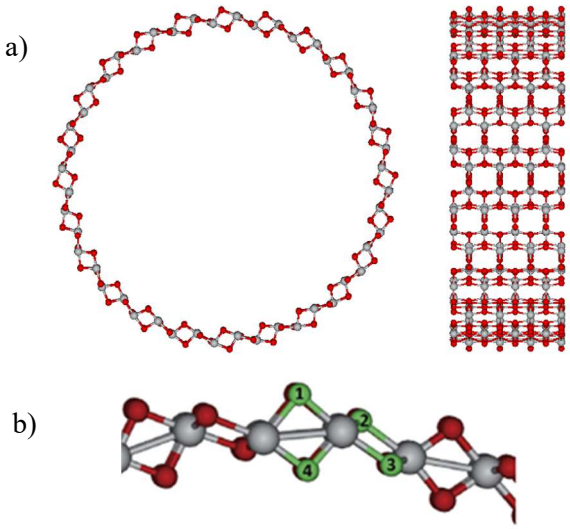

Figure 7. Schematic image of a 6-layer TiO_2(101) NT (a) with chirality indexes (-12,12): (top and lateral views). Ti atoms are shown in grey, O atoms in red, while outer substitutional atoms in yellow. The "basic" UC of (101) nanotube is repeated by 6 roto-translational symmetry operators. Numbered oxygen atoms shown as green (b) present different substitutional sites for N or S monodopant atoms.

In all cases sulphur dopants show a trend to be displaced from their initial substitution positions. Obviously, it is easier to follow such displacement from initial *S*1 and and S4 positions (Figure 7b). For sulphur substitutes, formation energies almost do not depend on S concentration, unlike N dopants, for which this dependence is noticeable, excluding external *N*1 site. Doping at *S*1 and *S*4 promotes the highest photocatalytic enhancement, reducing the gap between the ε_{LUIL} and ε_{HOIL} states, from 4.19 eV to 3.14 eV (3.12 eV) *vs*. 3.08 eV (3.07 eV) for 1.4% (2.8%) defect concentrations, respectively. It means that S-induced occupied levels have been found to be lower at 1.4% concentration. Unlike S-doped NTs, N dopants do not induce visible shift in positions of the VB top and CB bottom levels, they are almost the same as for the pristine NTs tructure. N dopants, however, induce empty states inside the band gap.

Photocatalytic suitability of N_O+S_O co-doped TiO_2 (101) NTs was found to be markedly higher than S and N mono-doped ones. Indeed, in the latter case, there are only four non-equivalent dopant positions (Figure 7b). Once one dopant is introduced, a number of options for different co-dopant sites appear. Due to limited computational resources, S dopant was put in its most preferable position, *S*1, while N dopants were inserted in different surrounding positions (as typed at the bottom of Figure 8).

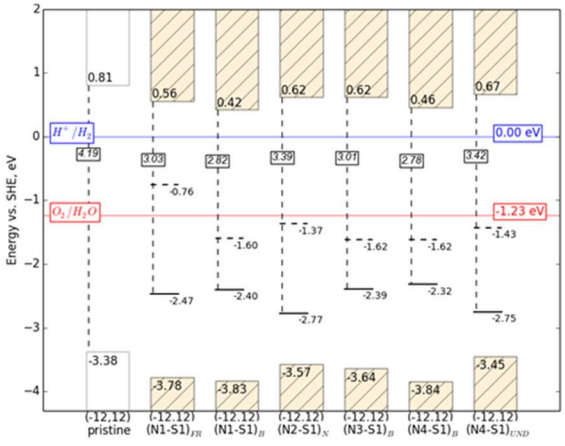

Figure 8. Schematic of the band edges and mid-gap states of pristine and N+S codoped 6-layered (-12,12) TiO_2(101) NTs (for 2.8% dopant concentration). Red and blue horizontal lines describe oxidation and reduction electrochemical potentials, respectively.

Photocatalytic suitability of Ag-, C- and N-doped wurtzite-structured [0001]-oriented prismatic ZnO nanowires: *Ab initio* evaluation

Yu.F. Zhukovskii, S. Piskunov, O. Lisovski

E. Spohr

Department of Theoretical Chemistry, University of Duisburg-Essen, Germany

R.A. Evarestov

Department of Quantum Chemistry, St. Petersburg State University, Petrodvorets, Russian Federation

Wurtzite-structured zinc oxide (ZnO) is considered in general as a promising photoelectrode for solar water splitting at the corresponding surface immersed in aqueous electrolyte. However, ZnO bulk samples, due to wide enough band gap (3.4 eV), can be considered as active for photocatalytic applications only under ultraviolet (UV) irradiation, where they possess ~1% efficiency of sunlight energy conversion. Although pristine zinc oxide prismatic nanowires (NWs) possess noticeably narrower band gaps than the corresponding bulk, the tendency of their reduction with increasing NW diameter was found to be still insufficient, thus, further structural modification is required to achieve photocatalytic suitability of ZnO NWs. To fill this gap, a series of *ab initio* calculations were performed on prismatic [0001]-oriented ZnO nanowires of different diameters, monodoped by metal (Ag) or non-metal atoms (C, N) with varied concentration (~3 *vs.* ~6%) and arrangement around nanowires (Figure 9).

In order to reproduce qualitatively the energies of one-electron states of doped ZnO nanowires, the hybrid DFT-HF Hamiltonian was used for large-scale first principles calculations based on the PBE0 exchange-correlation functional. Changes in the electronic structure induced in a few defect composition scenarios clearly show that, for specific concentrations and locations of the dopants, the optical absorption peak of doped ZnO can be shifted to the visible light range with promising efficiency. In agreement with experimental observation, the most significant results have been achieved for C-doped ZnO nanowires. They possess the highest photocatalytic suitability, since the band gap was reduced in this case down to 2.1–2.2 eV (for nanowire diameters of 2.9–3.5 nm), which corresponds to optimal 15–17% efficiency of solar energy conversion.

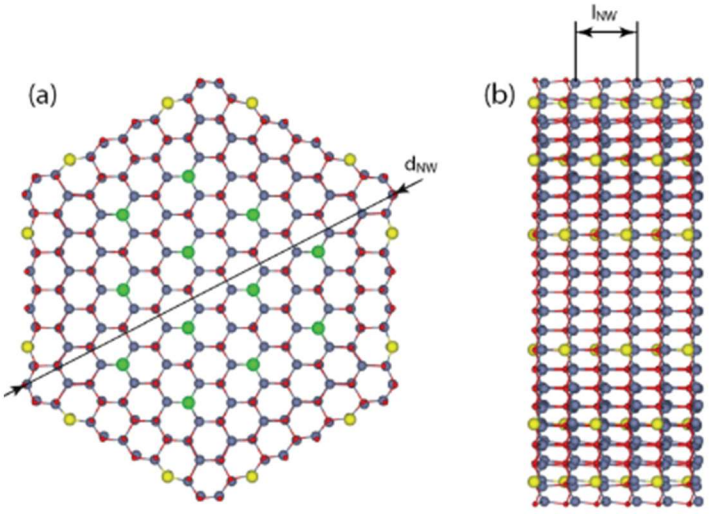

Figure 9. Cross-sectional (a) and lateral (b) images of the doped wurtzite-based hexagonal-shaped ZnO nanowire extended by 6×6 atomic shells around the hollow-centered [0001]-oriented axis, containing 216 formula units (or $432=12\times6^2$ atoms) *per* NW unit cell. The diameter and period of a nanowire are shown by the double arrows d_{NW} (a) and l_{NW} (b), respectively. An example of defect distribution at 3% concentration in a ZnO NW unit cell is given. Zn and O atoms are shown as small red and middle blue-grey balls, respectively. Outer (yellow) or inner (green) balls correspond to arrangement of Ag, C and N mono-dopants or O vacancies.

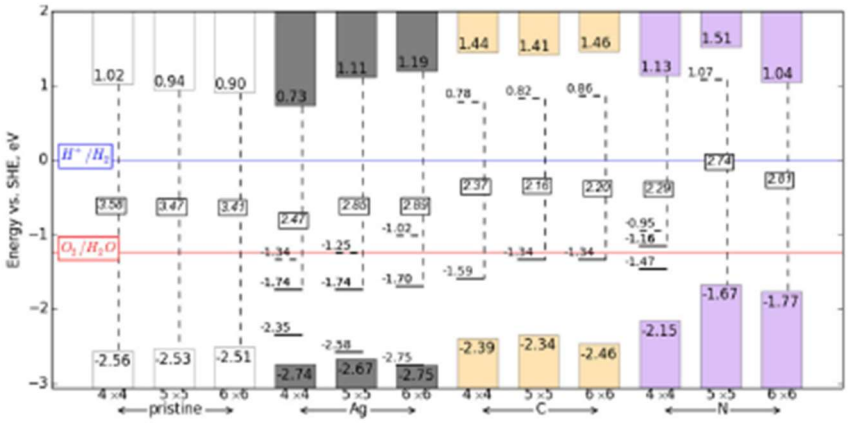

Figure 10. Energy diagram for pristine and doped ZnO NWs with ~6% defect concentration depending on d_{NW}. The red and blue horizontal lines correspond to the redox ε_{O_2/H_2O} and ε_{H^+/H_2} potentials, respectively. The zero of the energy scale corresponds to the standard hydrogen electrode (SHE) level. Solid and dashed horizontal lines describe the induced ε_{HOIL} and ε_{LUIL} levels, respectively.

The energy diagram shown in Figure 10 for different d_{NW} diameters and 6% defect concentration clearly demonstrates the highest photocatalytic suitability of C-doped nanowires with 5×5 and 6×6 thicknesses (their reduced band gaps correspond to 2.18 and 2.20 eV, respectively) as compared to pristine as well as Ag- and N-doped ones.

Epitaxial growth of $WS_2(0001)$ monolayers on $\{1\bar{1}00\}$ facets of wurtzite-structured ZnO nanowires: Experimental study and theoretical simulation

S. Piskunov, Yu.F. Zhukovskii

B. Polyakov, A. Kuzmin, K. Šmits, J. Zideluns, E. Butanovs, J. Butikova
Institute of Solid State Physicsy, University of Latvia, Riga

S. Vlassov
Institute of Physics, University of Tartu, Estonia

Core–shell nanowires (NWs) are perspective radially heterostructured nanomaterials which epitaxial growth can be realized even at noticeable core–shell lattice mismatch. Hexagonally shaped shell consisting of WS_2 nanolayers was grown on $\{1\bar{1}00\}$ facets of prismatic wurtzite-structured [0001]-oriented ZnO NWs (Figure 11). The morphology and phase composition of synthesized ZnO/WS_2 core–shell NWs were confirmed by scanning and transmission electron microscopy, micro-Raman, and photoluminescence spectroscopy.

Epitaxial growth of a few $WS_2(0001)$ monolayers on the $\{1\bar{1}00\}$ NW facets is unexpected due to incompatibility of their symmetry and structure. In order to relax this incoherence, a model of WS_2-containing bridging groups inside core-shell ZnO/WS_2 NW interface was proposed to perform large-scale *ab initio* simulations and to support its feasibility.

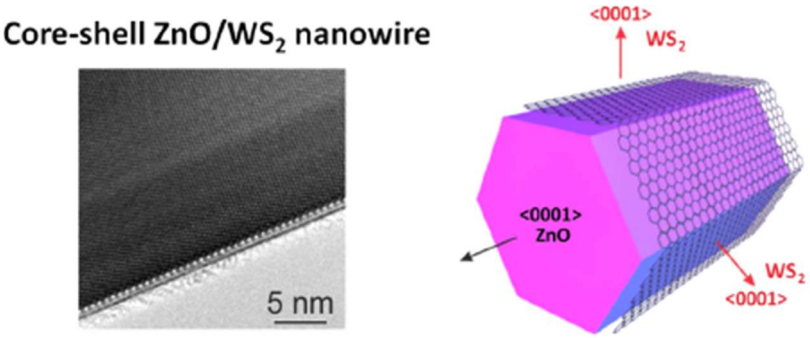

Figure 11. Transmission electron microscopy (TEM) image (left) and structural model of newly synthesized hexagonal-prism-shaped, wurtzite-structured and [0001]-oriented ZnO nanowire covered by epitaxially grown WS_2 monolayers.

Regular hexagonal prismatic shape of wurtzite-structured ZnO NWs can be formed if the NW axes are oriented along [0001] crystallographic directions being hollow-centered. Otherwise their symmetry described by $P6_3mc$ rod group will be reduced while stability (when NW is terminated by lateral facets possessing the smallest surface energy among any wurtzite faces) is lowered. This requirement is fulfilled for the family of six identical $\{1\bar{1}00\}$, $\{\bar{1}100\}$, $\{10\bar{1}0\}$, $\{\bar{1}010\}$, $\{01\bar{1}0\}$, and $\{0\bar{1}10\}$ ZnO facets (Figure 11). Alternative $\{11\bar{2}0\}$ faceting of [0001]-oriented ZnO NW was found to be energetically less favorable (by ~0.2 eV).

Large enough diameters (>50 nm) of ZnO NWs synthesized using the CVD method allowed us to assume that the key role in epitaxial WS_2 layer adhesion to nanowire is played by a family of $(1\bar{1}00)$ planes but not by tiny areas around ZnO NW ribs. This is why the 2D ZnO$(1\bar{1}00)$/WS_2 interface was selected for comparison with the experimental data for ZnO/WS_2 core-shell NWs. Since the latter cannot be atomistically simulated in principle when using the first-principle theory (due to a complexity of their morphology and essentially reduced symmetry) a 20-layer ZnO$(1\bar{1}00)$ slab model.was chosen for simulations of zinc oxide substrate (Figure 12b,c), thickness of which corresponds to [0001]-oriented NW possessing diameter of ~3.5 nm.

Both relaxed 3D models of ZnO and WS_2 lattices as well as 2D ZnO$(1\bar{1}00)$/WS_2 interfaces were calculated using the periodic hybrid DFT−HF Hamiltonian (exchange-correlation functional PBE0) as implemented in CRYSTAL code.

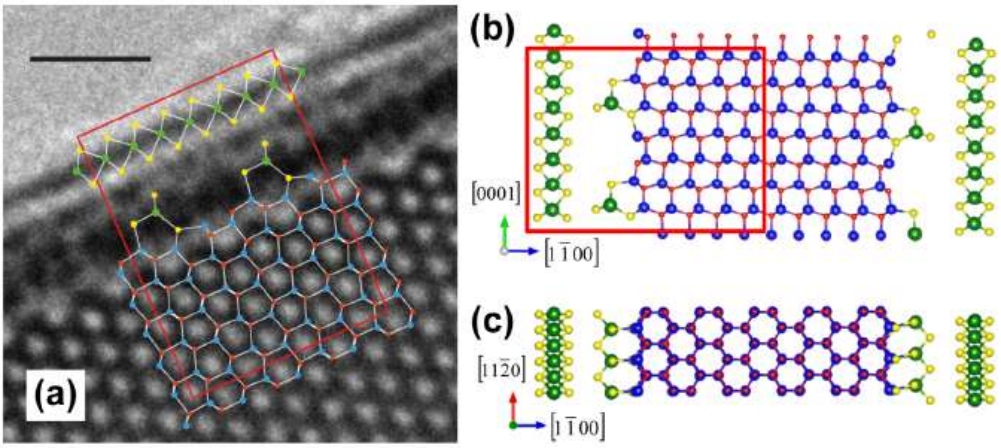

Figure 12. Imposition of optimized atomistic model of ZnO$(1\bar{1}00)$/striped 0.5 ML $WS_2$$(1\bar{1}00)$/$WS_2$(0001) interface on top of the TEM image of ZnO/WS_2 core-shell NW (scale bar is 1 nm) and sections of the same interface across (b) $(11\bar{2}0)$ and (c) (0001) planes. All three atomistic models contain WS_3 bridging groups.

Neutral and charged oxygen atom interstitials in corundum crystal: First principles simulations

A. Platonenko, D. Gryaznov, S. Piskunov, Yu.F. Zhukovskii, E.A. Kotomin

Combining a 2×2×1 supercell corundum model (consisting of 72 oxygen anions and 48 aluminium cations in their regular lattice sites) and hybrid B3PW exchange-correlation functional, large-scale *ab initio* LCAO calculations on both quasi-stable dumbbell configuration of interstitial neutral O_i^0 atom and charged O_i^- ion configuration in α-Al_2O_3 (corundum) crystal and possible migration trajectories have been modelled. Lattice distortion around quasi-metastable and migrating oxygen interstitials were optimized including

determination of the relaxed interatomic distances. The effective atomic charges and redistributions of the electronic density in O impurity-containing corundum were estimated too. Unlike the neutral O_i^0 interstitial atom forming dumbbell $O_i^0 - O_{reg}^{q-}$ configurations along migration trajectories (Figure 13), the charged O_i^- interstitial does not form dumbbells with the nearest regular O_{reg}^{q-} anion (Figure 14), due to the stronger repulsion between them and Coulomb attraction to the ne Al_{reg}^{q+} cations. Thus, three types of oxygens can be considered in α-Al_2O_3 lattice in absence or presence of interstitial impurity (Figure 15).

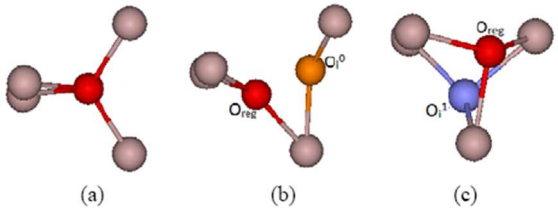

Figure 15. Reference oxygen sites in (a) perfect corundum crystal, (b) that containing neutral oxygen interstitial leading to the dumbbell formation $O_i^0 - O_{reg}^{q-}$ ($d_{O_i\text{-}O_{reg}}$ = 1.40 Å), (c) that containing charged oxygen interstitial ($d_{O_i^- - O_{reg}}$ = 1.87 Å). All views are shown across the vertical z-axis (Al ions oriented along them).

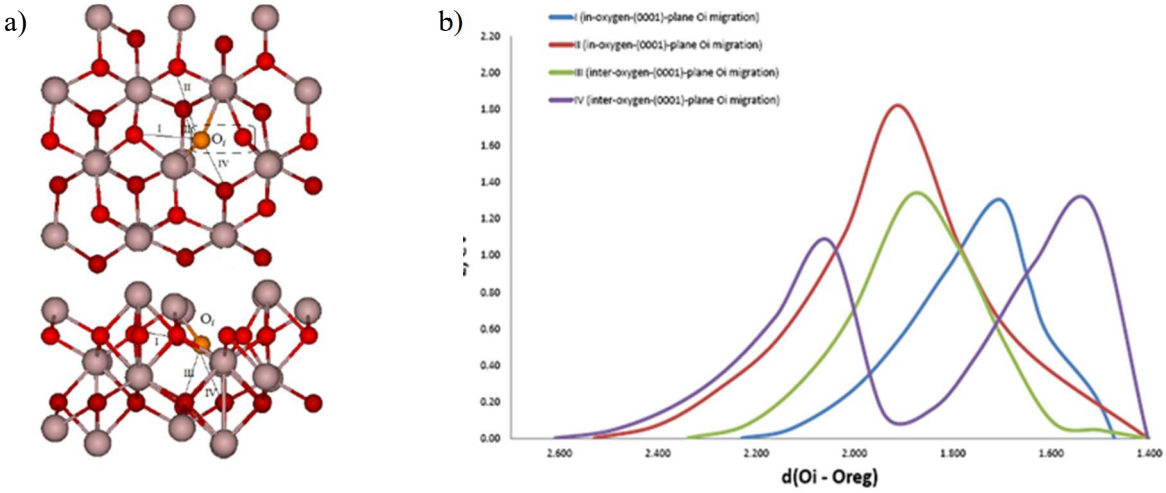

Figure 13. Atop (0001) and aside views of four migration paths I-IV for neutral O_i^0 impurity atom (shown as an orange ball) in α-Al_2O_3 lattice (a). Small red and large brown-gray balls correspond to O and Al atoms, respectively. Dumbbell (O_i-O_{reg}) pair is shown by a dotted rectangle. The energy curves for four migration paths I, II, III and IV of interstitial O_i^0 atom in corundum (b) and estimated energy barriers (transition states).

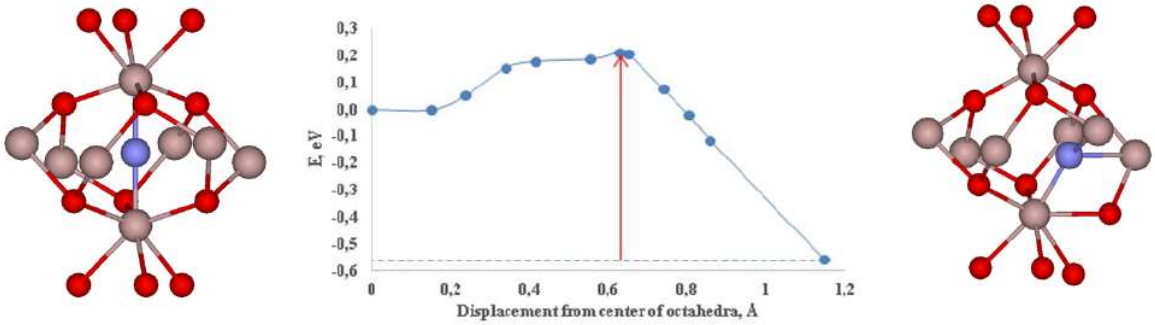

Figure 14. The potential energy curve for migration of interstitial O_i^- ion (shown as a blue ball) in corundum lattice. Zero point corresponds to its initial position in a centre of octahedron formed by six nearest O_{reg}^{q-} anions (left image), while the distance is counted from this centre to a final position (right image). The total height of the energy barrier for O_i^- ion is 0.76 eV being essentially smaller in comparison with the corresponding energy barrier of interstitial O_i^0 atom in α-Al_2O_3 lattice (~1.3 eV).

Large-scale plane-wave DFT calculations necessary for modeling of Y–O precipitate formation in γ-Fe lattice

A. Gopejenko, Yu.F. Zhukovskii, Yu.A. Mastrikov, E.A. Kotomin

P.V. Vladimirov, A. Möslang

Institut für Angewandte Materialien, Karlsruhe Institut für Technologie, Karlsruhe, Germany

V.A. Borodin

Nuclear Research Center Kurchatov Institute, Moscow, Russian Federation

Numerous experiments and theoretical studies clearly show that after high-temperature (>1000 C) mechanical alloying of steel and yttria a significant part of Y and O atoms is distributed in γ-Fe matrix with concentration above their equilibrium solubility. This might mean that nucleation and growth of Y_2O_3 clusters occurs already during the hipping stage in *fcc*-Fe phase.

Ab initio calculations of Y and O impurity atoms as well as V_{Fe} vacancies in the γ-Fe lattice were performed in order to describe the interactions between these defects, which are important for understanding of nanoparticles' formation within the oxide dispersed strengthened (ODS) steels. Large scale DFT calculations performed using plane-wave approach (as realised in VASP computer code) show that V_{Fe} vacancies considerably influence the binding between the impurity atoms. The results of performed calculations provide the detailed information about the binding energies between the defects, the changes of their effective charges and displacements of the substitute atoms relatively the host atom positions. The energy barriers necessary for the migration trajectories of impurity atoms in the γ-Fe lattice were found by performing the large-scale DFT calculations within the nudge-elastic band (NEB) method.

There is a strong repulsion between oversized yttrium solute atoms (at least their diameters essentially exceed those of iron atoms), which unavoidably leads to appearance of V_{Fe} vacancies close to newly-formed Y_{Fe} substitutes. Moreover, the latter willingly collect these vacancies in order to reduce the elastic relaxations of the lattice in their neighbourhood while the former can be occupied later by oxygen atoms (O_{Fe} substitutes) captured there from adjacent octahedral and tetrahedral interstitial sites in *fcc*-lattice. Due to lower energy barriers, O atom migrates much faster than Y, which is a limiting factor of Y–O precipitate growth inside iron matrix. In any case, adjacent O_{Fe} and Y_{Fe} substitutes can create in *fcc*-lattice different types of Y–O bonds (Figure 15).

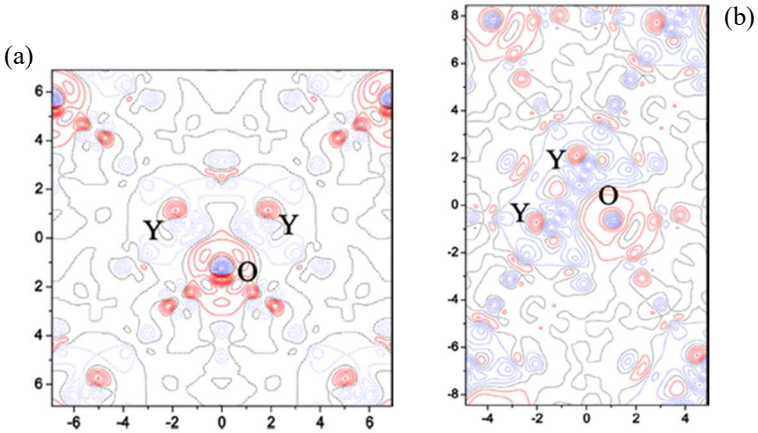

Figure 15. Difference electron charge density map for 2NN Y_{Fe}–O_{Fe}–Y_{Fe} (a) and 1NN Y_{Fe}–O_{Fe}–Y_{Fe} (b) configurations for Y_{Fe} atoms, whereas oxygen substitute atom is the first nearest neighbor for both Y atom pairs. Solid (red), dashed (blue) and dash-dotted (black) isolines (with the increment of 0.032 e Å^{-3}) represent positive, negative and neutral electronic charge, respectively.

Quantum chemical and molecular dynamical calculations on the electronic structure and lattice dynamics of ScF_3

D. Bocharov, S. Piskunov

P. Žguns, A. Kuzmin, and J. Purans
Institute of Solid State Physics, University of Latvia, Riga

M. Krack
Paul Scherrer Institute, Laboratory for Reactor Physics and Systems Behaviour, Villigen, Switzerland

A. Kalinko
Universität Paderborn, Naturwissenschaftliche Fakultät, Department Chemie, Paderborn, Germany

R.A. Evarestov
Department of Quantum Chemistry, St.Petersburg State University, St. Petrodvorets, Russian Federation

Sh.E. Ali
Physics Department, Faculty of Science, Suez Canal University, Ismailia, Egypt

F. Rocca
IFN-CNR, Institute for Photonics and Nanotechnologies, Unit FBK-Photonics of Trento, Povo, Italy

Scandium fluoride ScF_3 is a perovskite-type crystal which possesses a simple cubic structure (Figure 16) and attracts enhanced attention due to its large negative thermal expansion (NTE) over a wide range of temperatures (0-1100 K).

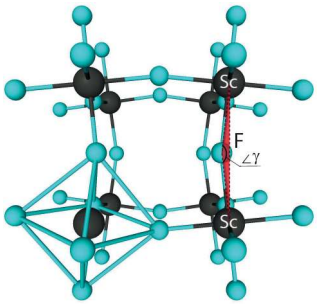

Figure 16. Prospective image of cubic ScF_3 lattice unit cell with parameter a_o equalled to the shortest Sc-Sc distance. Angle γ corresponds to the deviation of joint Sc-F bonds from the vertical direction. ScF_6 octahedron around the left bottom Sc atom corresponds to the primitive unit cell.

The electronic structure, lattice dynamics, and phonon anharmonicity of ScF_3 crystal were studied within the framework of quantum chemistry approaches (LCAO, hybrid HF-DFT) using Crystal09 and VASP computer codes. *Ab initio* hybrid electronic structure calculations were found to be able to reproduce qualitatively well the experimental values of lattice parameter (a_0 = 4.0257 Å at T = 0 K). The width of band gap (ε_{gap} > 8.9 eV) also confirms available experimental data. Calculated partial density of electron states (PDOS) is also in good agreement with valence-band photoelectron as well as the F 1*s* X-ray absorption spectra available in literature. The total density of phonon states determined within quasi-harmonic approximation from phonon dispersion curves and calculated along the high-symmetry directions Γ-X-M-R-Γ of the Brillouin zone, agrees reasonably well too.

At the same time, the temperature dependence of the experimentally measured infra-red (IR) absorption spectra, consisting of two bands at 220 and 520 cm^{-1} cannot be explained within the quasi-harmonic approach, which predicts shifts of these bands in an opposite direction relatively to that experimentally observed. To resolve this issue, a simple model was developed based on the symmetry analysis of phonon modes and use of the temperature-dependent experimental results of diffraction and EXAFS studies. Suggested model allows us to reproduce the unexpected experimental behavior observed for two bands in the IR absorption spectrum of ScF_3 and can be also applied for the interpretation of its other spectroscopic properties.

Calculations on ScF_3 bulk performed using CP2K code package demonstrated efficiency of the MD-EXAFS approach in combination with *ab initio* molecular dynamics for theory validation and description of temperature-dependent structural properties for ScF_3. Within this

approach configuration-averaged Sc *K*-edge EXAFS spectra were reproduced using molecular dynamics with NVT ensemble for three different temperatures (T = 300 K, 600 K and 1000 K) as well as compared with the experimental data suggesting a good qualitative agreement. It was found that upon temperature increase the ScF_6 octahedra do not behave as rigid units: the strong rotation of ScF_6 octahedra is accompanied by their expansion caused by the anharmonic Sc-F bonding, despite of a negative thermal expansion of ScF_3 crystalline lattice.

Interpretation of the U *L*3-edge EXAFS in UO_2 using molecular dinamics and plane-wave density functional theory calculations

D. Bocharov, E.A. Kotomin

A. Kuzmin, J. Purans
Institute of Solid State Physics, University of Latvia, Riga

M. Krack, M. Chollet, J. Bertsch, D. Grolimund, M. Martin
Paul Scherrer Institute, Laboratory for Reactor Physics and Systems Behaviour, Villigen, Switzerland

The experimental U *L*3-edge EXAFS spectra of uranium dioxide were interpreted up to 6 Å in *R*-space using the results of both classical and *ab initio* molecular dynamics simulations (CMD and AIMD, respectively) as well as taking into account the multiple scattering effects.

The accuracy of CMD method relies on the used force-field model; therefore EXAFS spectra can be employed for its further validation. Nine different force-field models of uranium dioxide differ mainly in description of the U-O vibrational amplitudes. Thus, the EXAFS data provide valuable information in order to evaluate the quality of the force-field modeling. The importance of the multiple-scattering contributions for the EXAFS analysis was also estimated. The obtained results suggest that they are not sufficiently large for UO_2 but remain still important in the range of the second (U2) and third (O3) coordination shells around uranium.

The advantage of the AIMD method is the absence of the adjustable parameters, except for the choice of the functional model. The exchange-correlation functional PBE employed in plane-wave DFT calculations on uranium dioxide predicts too rigid interactions.

The Cr *K*-edge XANES was simulated within the full-multiple-scattering formalism considering a substitutional model (Cr at U site). The analysis of the Cr K-edge XANES spectrum of Cr-doped UO_2 suggests that the substitutional model (Cr_U site) differs from experimental data, even when structure relaxation is considered. Therefore, further investigations are required to shed light on accommodation of Cr atoms and precipitates within the UO_2 host lattice.

B. Kinetics of processes with self-organization

Theoretical analysis of defect recombination kinetics in insulators

V.N. Kuzovkov, E.A. Kotomin, A.I. Popov, A.M. Moskina,

E. Vasil'chenko and A. Lushchik,
Institute of Physics, University of Tartu, Estonia

R. Vila
CIEMAT, Madrid, Spain

As is well known, irradiation of insulating crystals results in formation of the primary complementary Frenkel defects – vacancies and interstitials (called in alkali halides as *F* and *H* centers) – which become mobile above some critical temperatures, and then either recombine or aggregate. Despite numerous experimental studies of the kinetics of primary defect annealing upon temperature increase obtained by a number of optical, magnetic methods, very little *quantitative*

information is available on the defect migration energies and their pre-exponential factors. These parameters are necessary for the prediction of possible secondary reaction kinetics and, in general, material radiation stability.

The experimental kinetics of the low-temperature diffusion-controlled *F* amd *H* center recombination was carefully analyzed in a series of irradiated alkali halides and oxides. As a result, the migration energies and pre-exponential parameters for the hole centers (called the color *H* center in alkali halides, and interstitial oxygen ions in aluminum oxides), were extracted.

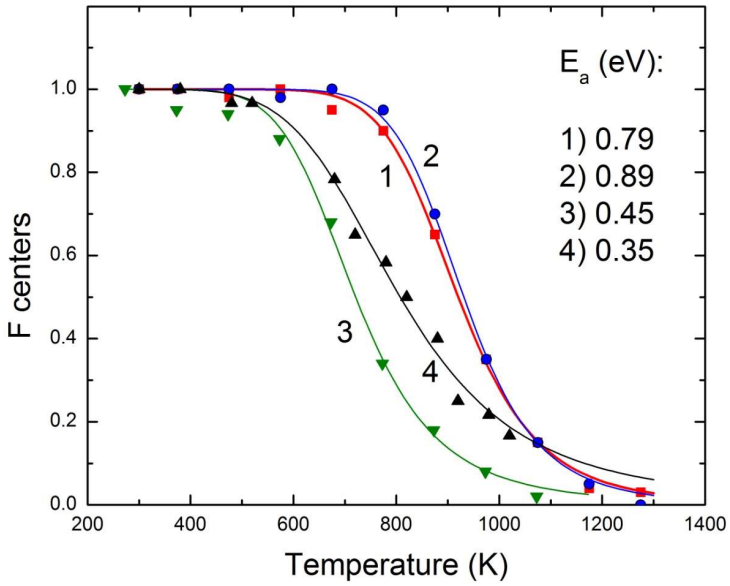

Figure 17. The experimental kinetics of *F* –type centers annealing in four different neutron irradiated Al_2O_3 samples. The full lines are drawn based on theory. The effective migration energies are shown in the legend.

In particular, a comparison of the calculated and experimental annealing kinetics for the *F* centers in both neutron irradiated and thermochemically reduced Al_2O_3 samples (Figure 17) allowed us to estimate the migration energy of interstitial oxygen ions and that for the *F* centers as ~0.8 eV and ~4.5 eV. The former energy was checked with that estimated by means of atomistic defect calculations (Section A) - a qualitative agreement was observed.

Kinetics of metal colloid formation in thermochemically reduced and heavily irradiated ionic solids

V.N. Kuzovkov, E.A. Kotomin, A.I. Popov

It is known that mobile *F* centers in alkali halides produce complex defects containing the dimer (*M* centers), trimer (*R*), tetramer (*N*) *F*-aggregates and finally, metal colloids. In particular, such kinetics was studied in hevily electron-irradiated NaCl crystals. It was shown that the *F* center concentration decay above 400 K is accompanied by a simultaneous growth of the *colloid* X-absorption band. In this case, the main mechanism of colloid formation is the mutual encounter of mobile *F* centers and their aggregation caused by an elastic attraction, which can be characterized by the interaction energy ε for the nearest neighbor defects. We developed the relevant theory and computer code.

Fig. 18 depicts the calculated annealing kinetics of F centers for different values of migration energy E_a and simultaneous temperature-induced growth of the concentration of colloids consisting of different number of defects (N_0) in a NaCl crystal. The best agreement with experimental data (filled squares) is achieved for $E_a = 1.13$ eV which is close to the previous estimates. It is commonly accepted that the peak energy and halfwidth of the X-absorption band of metal colloids depend strongly on colloid size: very small colloids possess broad structureless bands, whereas the well-pronounced experimental optical band presented in Fig. 18 definitely corresponds to large-size colloids. We assume here the Poisson distribution of colloids in size. Fig. 18 shows that the best agreement with experimental data is achieved assuming that each colloid contains at least $N_0 = 20$ defects.

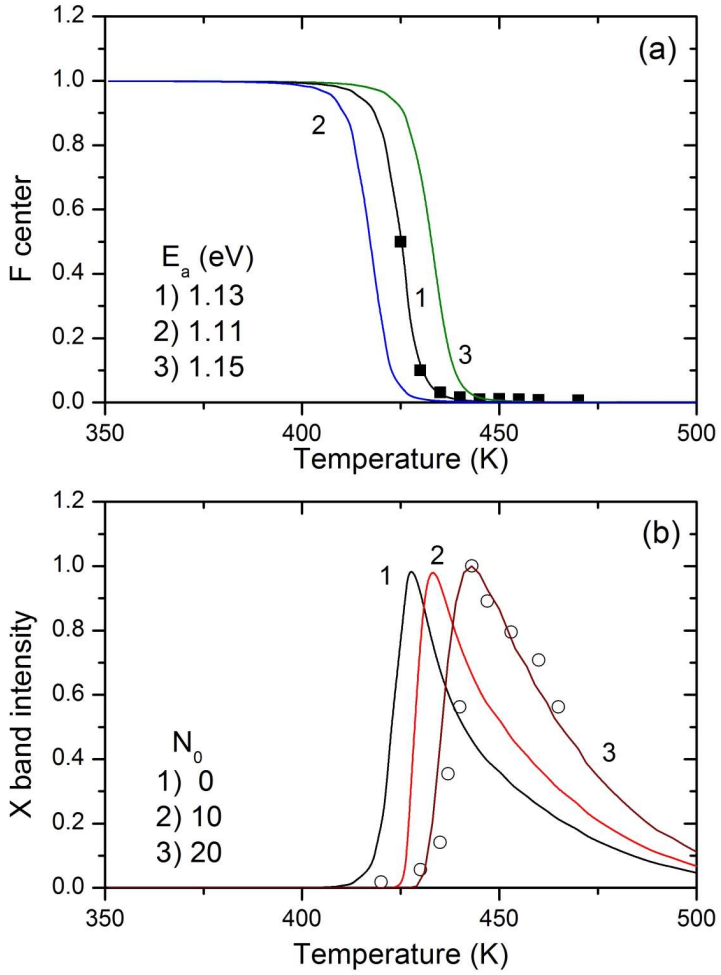

Figure 18. The calculated annealing kinetics (solid lines) of the F center concentration in NaCl for different values of migration energies E_a (a) as well as the growth of the colloid concentration with the certain defect number N_0 (b). The experimental points are shown by filled squares (a) and open circles (b).

We performed also calculations for Al colloids in corundum which arise in thermochemically reduced corundum during annealing above 1700 K. The Al colloids are predicted here to be quite small, 10-20 Å, in agreement with the available experiments.

Stabilization of primary mobile radiation defects in MgF_2 crystals

A.I. Popov, E.A. Kotomin

V.M. Lisitsyn, L.A. Lisitsyna
National Research Tomsk Polytechnic University, Russia

F.U. Abuova, A.T. Akilbekov,
L.N. Gumilyov Eurasian National University, Astana, Kazakhstan

J. Maier
Max Planck Institute for Solid State Research, Stuttgart, Germany

Non-radiative decay of the electronic excitations (excitons) into point defects (*F*-*H* pairs of Frenkel defects) is main radiation damage mechanism in many ionic (halide) solids. Typical time scale of the relaxation of the electronic excitation into a primary, short-lived defect pair is about 1–50 ps with the quantum yield up to 0.2-0.8. However, only a small fraction of these primary defects are spatially separated and survive after transformation into stable, long-lived defects.

The survival probability (or stable defect accumulation effeciency) can differ by orders of magnitude, dependent on the material type; *e.g.*, ~10% in alkali halides with *fcc* or *bcc* structure, 0.1% in rutile MgF_2 and <0.001% in fluorides MeF_2 (Me: Ca, Sr, Ba). The key factor determining accumulation of stable radiation defects is stabilization of primary defects, first of all, highly mobile hole *H* centers, through their transformation into more complex immobile defects.

Theoretical calculations of the migration energies for *F* and *H* centers were perofrmed in poorely studied MgF_2 crystals with a focus on the *H* center stabilization in the form of the interstitial F_2 molecules (Figure 19) which is supported by presented experimental data. Formation of these very stable and optically inactive molecules (unlike X_3^- complex hole *H* centers in alkali halides) explains peculiarities of the radiation stability of MgF_2 crystals.

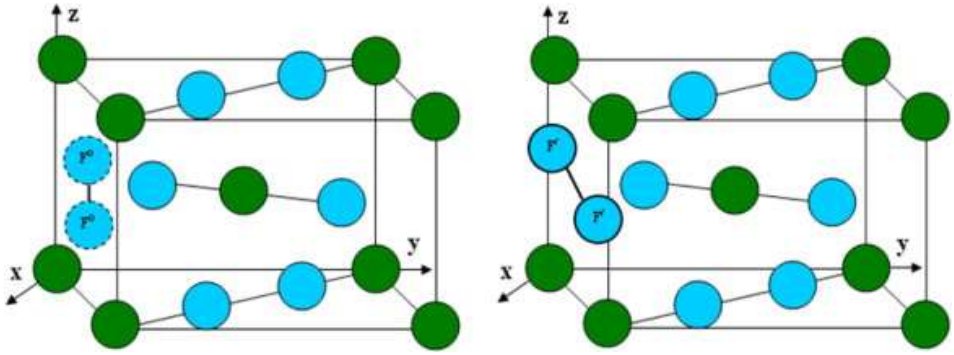

Figure 19. The initial (left) and optimized (right) configurations of interstitial F_2 molecule in a rutile MgF_2 structure.

Void lattice formation in electron-irradiated CaF_2: Statistical analysis of experimental data and celullar automata simulations

G. Zvejnieks, V.N. Kuzovkov, E.A. Kotomin, P. Merzlyakov

Calcium fluorite (CaF_2) is an important optical material widely used in both microlithography and deep ultraviolet (UV) windows. It is well known that under certain conditions the electron beam irradiation can create therein a super-lattice consisting of vacancy clusters (called a *void lattice*). The goal of this study is the two-fold.

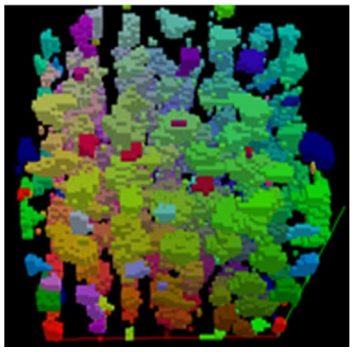

Figure 20. Snapshot of the cellular automata modelling of the *F, H* center formation in CaF_2 (voids are red, interstitials green).

Firstly, to perform a quantitative analysis of experimental TEM images demonstrating void lattice formation, we developed two distinct image filters. As a result, we can easily calculate vacancy concentration, vacancy cluster distribution function as well as average distances between defect clusters. The results for two suggested filters are similar and demonstrate that experimental void cluster growth is accompanied by a slight increase of the void lattice constant.

Secondly, we proposed a microscopic model that allows us to reproduce a macroscopic void ordering, in agreement with experimental data, and to resolve existing theoretical and experimental contradictions (Figure 20). Our computer simulations demonstrate that macroscopic void lattice self-organization can occur only in a narrow parameter range. Moreover, we studied the kinetics of a void lattice *ordering*, starting from an initial disordered stage, in a good agreement with the TEM experimental data.

A novel quantum field approach to photoexcited insulators

E. Klotinsh

In order to predict optical properties of insulating materials under intensive laser excitation, methods of quantum electrodynamics were generalized, which allowed us to simulate excitation of electrons and holes, interacting with each other and acoustic phonons.

The prototypical model considers a two-band dielectric material which is characterized by the dispersion relations for the electron and hole states. Universal description of the excited electrons, holes and acoustic phonons was developed within the formalism of a joint quantum kinetics.

Illustrative solutions for the quasiparticle birth-annihilation operators, applicable at short laser pulses at 0 K, were obtained by the transition from the macroscopic description to the quantum field formalism.

C. Plasma Physics

Self-consistent non-stationary theory of gyrotrons

O. Dumbrajs

G.S. Nusinovich
Institute for Research in Electronics and Applied Physics,
University of Maryland, College Park, USA

For a long time, the gyrotron theory was developed assuming that the transit time of electrons through the interaction space is much shorter than the cavity fill time. Correspondingly, it was assumed that during this transit time the amplitude of microwave oscillations remains constant. A recent interest to such additional effects as the after-cavity interaction between electrons and the outgoing wave in the output waveguide had stimulated some studies of the beam-wave interaction processes over much longer distances than a regular part of the waveguide which serves as a cavity in gyrotrons. Correspondingly, it turned out that the gyrotron theory free from the assumption about constant amplitude of microwave oscillations during the electron transit time should be developed. The present study presents some results obtained in the framework of such theory.

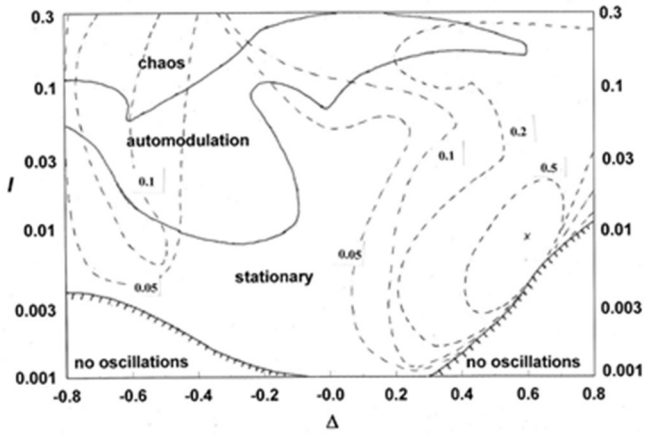

Figure 21. Zones of different kinds of oscillations are separated by solid lines. The normalized interaction length μ = 15 allows realizing the maximum orbital efficiency. The contours of constant orbital efficiencies are shown by dashed lines. The point of the maximum orbital efficiency 0.7 is marked by the cross.

The main attention is paid to modification of the boundary between the regions of oscillations with constant amplitude and auto-modulation in the plane of normalized parameters characterizing the external magnetic field and the beam current (Figure 21). It is shown that the theory free from the assumption about the frozen wave amplitude during the electron transit time predicts some widening of the region of auto-modulation.

Hysteresis and frequency tunability of gyrotrons

O. Dumbrajs,

E.M. Khutoryan
Institute for Radio Physics and Electronics, Kharkiv, Ukraine

T. Idehara
Research Center for Development of Far-Infrared Region, University of Fukui, Japan

We presented the first devoted theoretical and experimental study of hysteresis phenomenon in relation to frequency tunability of gyrotrons. In addition, we generalized theory describing electron tuning of frequency in gyrotrons developed earlier, to arbitrary harmonics. It is found that theoretical magnetic and voltage hysteresis loops are about twice larger than experimental loops. In gyrotrons whose cavities have high quality factors hysteresis allows one only little to broaden the frequency tunability range.

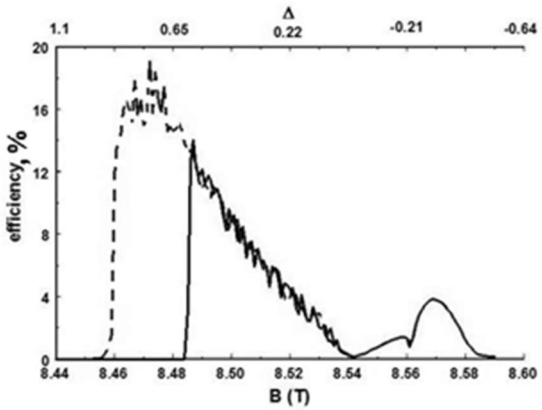

Figure 22. Efficiency as a function of magnetic field. On the upper ordinate axis frequency mismatch Δ is shown. Calculations were started at *8.44 T* and finished at *8.59 T*. Oscillation appears at *8.483 T* and disappears at *8.59 T* (solid curve). On the way back, oscillation disappears at *8.455 T* (dashed curve). Here *I=0.4 A* and *U=20 kV*. Hence, a large hysteresis region is observed between $8.455T$ and $8.483T$.

Start-up scenario of a high-power pulsed gyrotron for 300 GHz band collective Thomson scattering diagnostics in a large helical device

O. Dumbrajs

T. Saito, Y. Tatematsu
Research Center for Development of Far-Infrared Region,
University of Fukui, Japan

We presented results of theoretical study of mode competition during the voltage rise of a 300-kW, 300-GHz gyrotron operating in the $TE_{22,2,1}$ mode. Simulations tracking eight competing modes show that, with a proper choice of the magnetic field, stable excitation of the operating mode can be realized, despite the presence of parasitic modes in the resonator spectrum. A finite voltage rise time, 1 kV/4 ns referred to as the slow voltage rise case, is taken into account to simulate realistically the experimental condition. Simulation results with the finite voltage rise time are in good agreement with the experimental test, in which the gyrotron demonstrated reliable operation at power levels up to 300-kW. Moreover, along with voltage rise, the oscillation manner changes from backward wave oscillation to gyrotron oscillation. In the range of the magnetic field lower than the magnetic field strength at which the $TE_{22,2}$ mode attains to the maximum power, mode competition with the $TE_{21,2}$ mode takes place although many other competing modes exist in between the two modes.

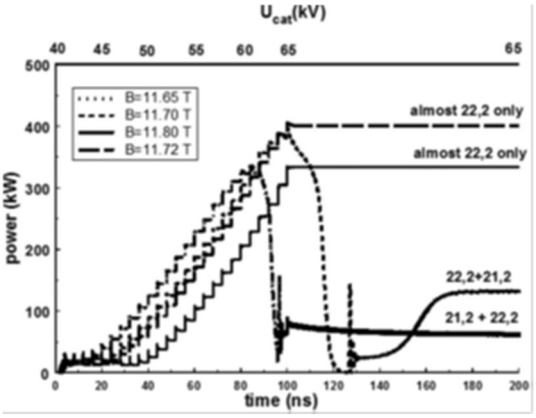

In addition to the slow voltage rise case, the fast voltage rise case, 10 kV/4 ns, and the instant voltage rise case were considered. For these cases, simulations also predict stabile oscillation of the $TE_{22,2}$ mode with the same power level with the slow voltage rise case. This indicates that stable oscillations of the $TE_{22,2}$ mode can be obtained in a wide range of the voltage rise time.

Figure 23. Output power for different magnetic fields as a function of time and voltage.

D. Experimental Studies

Cathodoluminescence characteriazaion of polysterene – $BaZrO_3$ hybrid composites

A.I. Popov, A. Moskina

V.P. Savchyn, O.I. Aksimentyeva, I. Karbovnyk, Yu.Yu. Horbenko
Ivan Franko National University of Lviv, Ukraine

H. Klym,
Lviv Polytechnic National University, Ukraine

V. Serga
Institute of Inorganic Chemistry, Riga Technical University, Latvia

Both inorganic and organic nanosystems based on the semiconductor nanocrystals and either conducting or thermoplastic polymers are prospective for a number of technological applications and, thus, attract nowadays enhanced attention.

$BaZrO_3$ (BZO) perovskite has found several applications, such as substrate for the synthesis of superconductors, high temperature microwave dielectrics, electrolyte for protonic fuel cells. We studied the effect of polymer matrix on the luminescent properties and the structure of hybrid composites based on suspension polystyrene (PS) and nanocrystals of BZO (d < 50 nm) have been studied using luminescent spectroscopy and XRD analysis.

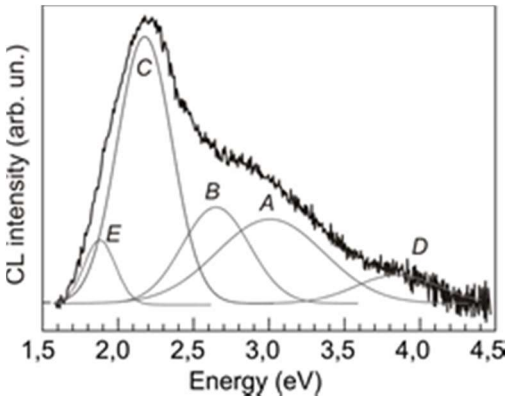

Figure 24. CL spectra of PS-BZO nanocomposite at RT.

A strong cathodoluminescence (CL) in BZO-nanocrystals is observed in temperatur range 80–293 °K. It is modified in BZO-PS composites: both the low- and a high-energy bands (near 4 eV) appear, together with a significant reduction in the CL intensity. A decrease of the lattice parameter a for BZO phas in the composite and the modification of CL spectra indicate for changes in the nanocrystalline structure induced by the polymer.

The PS-BZO composites show the modification of the CL spectrum. The Gaussian decomposition of CL curves shows that the additional lowest energy band E and the highest energy band D (near 4 eV) arise, accompanied with a significant reduction in the CL intensity. As seen from a comparison of CL spectra of BZO–PS composites with nano-BZO (Figure 24) as well as micro-BZO, the ratio between the intensities of the lower energy CL bands and higher ones strongly depends on the BZO grain size.

Photostimulated luminescence properties of neutron image plates

A.I. Popov

J. Zimmermann[1,2]

[1] *Institut für Materialwissenschaft, Technische Universität Darmstadt, Germany*
[2] *Fraunhofer-Institut für Silicatforschung ISC, Alzenau, Germany*

G.J. McIntyre[3,4], C. Wilkinson[3]

[3] *Institut Laue-Langevin, Grenoble, France.*
[4] *The Bragg Institute, ANSTO, Australia*

The luminescence properties of two commercial neutron-sensitive image-plates based on Gd_2O_3-doped BaFBr:Eu^2 storage phosphors are examined. These are white Fuji plates and blue Fuji plates (BAS-ND) with Gd_2O_3 content by weight of 34% and 50%, respectively (Figure 25). Both plates show two maxima in the photostimulation spectrum near 500 nm and 600 nm, with the ratio of the peak responses ($I_{600\ nm}/I_{500\ nm}$) 1.39 and 0.53 for the white and blue plates, respectively.

The optimum wavelengths for photostimulation for the two phosphors are therefore different. The response of the blue plate is only 25% that of the white plate, if each is stimulated at its optimum wavelength.

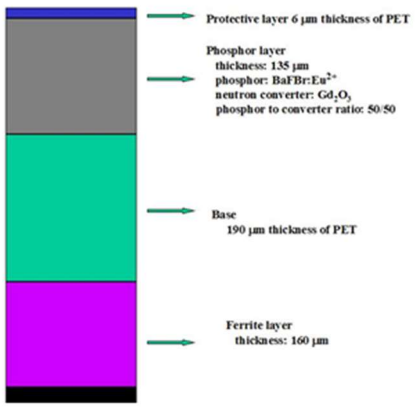

Figure 25. Structure of BAS-ND neutron image plate.

From Figure 26 we can see that the relative PSL intensity of the White NIP is 5.25 times higher than that of the Blue NIP, when the plates are stimulated with a wavelength corresponding to that of a He-Ne laser. The dye contained in the Blue NIP's will also absorb stimulating photons in the red region of the spectrum, which in turn could produce less stimulated luminescence. The better response of the White plates could also be because they contained more storage phosphor than the Blue plates and that $F(Br^-)$-centers are more efficiently created in its storage phosphor.

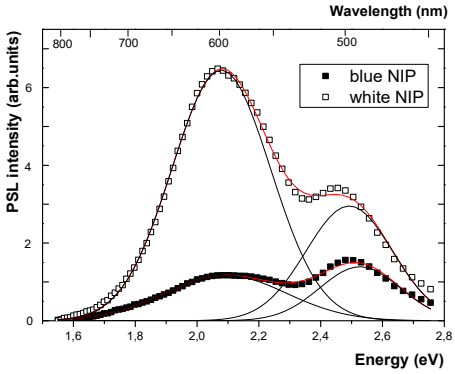

Figure 26. Stimulation spectra of X-ray irradiated Blue and White NIP's and their Gaussian deconvolution. The stimulation spectra were observed by measuring the PSL emission of Eu^{2+} at about 400 nm.

Long-term evolution of luminescent properties in CdI_2 crystals

A.I. Popov

I. Karbovnyk, I. Bolesta, I. Rovetskyi, V. Lesivtsiv, Ya. Shmygelsky, S. Velgosh

Department of Electronics, Ivan Franko National University of Lviv, Ukraine

Fresh and aged melt-grown or gas-phase grown CdI_2 crystals are studied by means of low-temperature photoluminescence spectroscopy. Noticeable transformations of emission spectra are observed after long-term aging.

Time evolution of the CdI_2 emission spectra at a long-term (several years) aging in air is shown in Figure 27. Freshly grown crystals (a bottom plot in Figure 27) show an intensive band peaked at 2.48 eV (501 nm, G-band) with a weak component on the long-wavelength shoulder (2.25 eV, 551 nm, Y-band). This emission does not depend on the excitation wavelength and is related to the radiative recombination of self-trapped excitons in $[Cd^{2+}I_6^-]^{4-}$ molecular complexes.

A specific feature of 1.87 eV this narrow band is its bandwidth of *FWHM* = 0.05 eV, which is dramatically different from that for other bands. It is plausible to assume that this band is related to CdO and $Cd(OH)_2$ nanoinclusions.

We have also examined the changes in the emission spectra of aged melt-grown and gas-phase-grown CdI_2 crystals (Figure 28). In both spectra the band at 1.87 eV is clearly identified, whereas there are some noticeable differences in the short-wavelength region of the spectra.

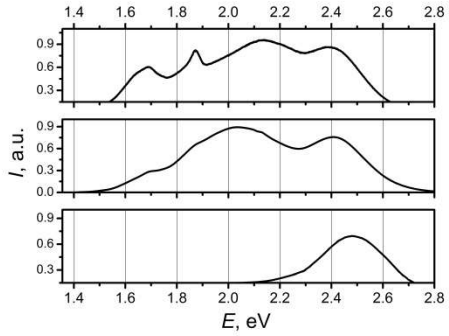

Figure 27. Photoluminescence spectra of freshly melt-grown (bottom), 2-year aged (middle) and 4-year (top) aged CdI_2 crystals. Spectra are recorded under excitation by 12.4 eV (100 nm) photons at 8 K.

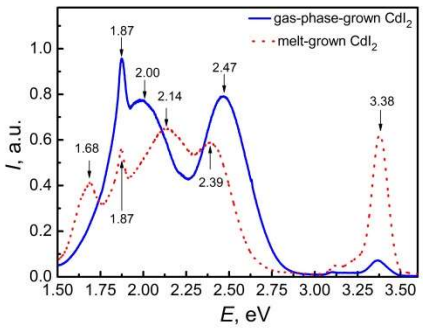

Figure 28. Luminescence spectra measured for melt-grown and gas-phase-grown CdI_2 crystals at the excitation by 12.4 eV photons at T = 8 K.

One of the reasons for these differences is the crystal thickness: melt-grown samples are found to be 0.1 to 0.5 mm thick, whereas the thickness of single-crystalline plates of gas-phase-grown CdI_2 does not exceed 10 microns. Thin crystals possess increased ratio of the number of surface atoms (N_s) to the number of bulk (N_v) atoms. Thus, surface atoms should have prevailing contribution to the optical properties of crystal. Geometrical order of atom distribution in the bulk (volume) and on the surface is also different (Figure 29). This conclusion is confirmed by nuclear quadrupole resonance (NQR) frequency studies of ^{127}I in CdI_2 crystals.

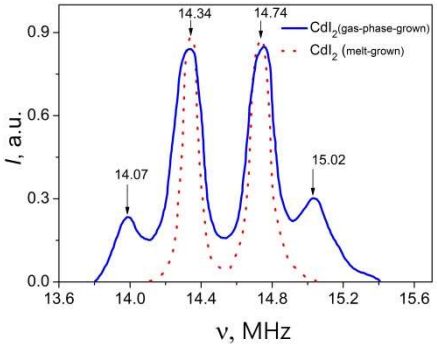

Figure 29. NQR spectra of ^{127}I isotopes in melt-grown and gas-phase-grown CdI_2 crystals.

==========

Publications in 2016

1. Bjørheim, T. S., Arrigoni, M., Saeed, S. W., **Kotomin**, **E.A**., and Maier, J. Surface segregation entropy of protons and oxygen vacancies in $BaZrO_3$. - *Chemistry of Materials*, *28*(5), p. 1363-1368 (2016). **SNIP**: **2.07.**

2. **Gryaznov**, **D.**, Merkle, R., **Kotomin**, **E.A**., and Maier, J. *Ab initio* modelling of oxygen vacancies and protonic defects in $La_{1-x}Sr_x FeO_{3-\delta}$ perovskite solid solutions. - *Journal of Materials Chemistry A*, *4*(34), p. 13093-13104 (2016). **SNIP: 1.62.**

3. **Dumbrajs, O.**, Khutoryan, E.M., and Idehara, T. Hysteresis and frequency tunability of gyrotrons. - *Journal of Infrared, Millimeter, and Terahertz Waves*, *37*(6), p. 551-560 (2016). **SNIP: 1.37.**

4. Polyakov, B., Kuzmin, A., Smits, K., Zideluns, J., Butanovs, E., Butikova, J., Vlassov, S., **Piskunov**, **S**., and **Zhukovskii**, **Yu**.**F**. Unexpected epitaxial growth of a few WS_2 layers on $\{1\bar{1}00\}$ facets of ZnO nanowires. - *The Journal of Physical Chemistry C*, *120*(38), p. 21451-21459 (2016). **SNIP: 1.23.**

5. Arrigoni, M., Bjørheim, T.S., **Kotomin**, **E**.**A**., and Maier, J. First principles study of confinement effects for oxygen vacancies in $BaZrO_3$ (001) ultra-thin films. - *Physical Chemistry Chemical Physics*, *18*(15), p. 9902-9908 (2016). **SNIP: 1.21.**

6. **Popov**, **A**.**I.**, Zimmermann, J., McIntyre, G.J., and Wilkinson, C. Photostimulated luminescence properties of neutron image plates. - *Optical Materials*, *59*, p. 83–86 (2016). **SNIP: 1.08.**

7. **Zvejnieks**, **G**., Merzlyakov, P., **Kuzovkov**, **V**.**N**., and **Kotomin**, **E**.**A**. Void lattice formation in electron irradiated CaF_2: Statistical analysis of experimental data and cellular automata simulations. - *Nuclear Instruments and Methods in Physics Research Section B: Beam Interactions with Materials and Atoms, 368*, p. 138-143 (2016). **SNIP: 0.98.**

8. **Piskunov**, **S**. and **Eglitis**, **R**.**I**. Comparative ab initio calculations of $SrTiO_3/BaTiO_3$ and $SrZrO_3/PbZrO_3$(001) heterostructures. - *Nuclear Instruments and Methods in Physics Research Section B: Beam Interactions with Materials and Atoms, 374*, p. 20-23 (2016). **SNIP: 0.98.**

9. Lisitsyn, V. M., Lisitsyna, L. A., **Popov**, **A**.**I**., **Kotomin, E.A.**, Abuova, F. U., Akilbekov, A., and Maier, J. Stabilization of primary mobile radiation defects in MgF_2 crystals. - *Nuclear Instruments and Methods in Physics Research Section B: Beam Interactions with Materials and Atoms*, *374*, p. 24-28 (2016). **SNIP: 0.98.**

10. **Zhukovskii**, **Yu**.**F**., **Platonenko**, **A**., **Piskunov**, **S**., and **Kotomin**, **E**.**A**. *Ab initio* simulations on migration paths of interstitial oxygen in corundum. - *Nuclear Instruments and Methods in Physics Research Section B: Beam Interactions with Materials and Atoms*, *374*, p. 29-34 (2016). **SNIP: 0.98.**

11. Lushchik, A., Lushchik, C., **Popov, A.I.**, Schwartz, K., Shablonin, E., and Vasil'chenko, E.. Influence of complex impurity centres on radiation damage in wide-gap metal oxides. - *Nuclear Instruments and Methods in Physics Research Section B: Beam Interactions with Materials and Atoms, 374*, p. 90-96 (2016). **SNIP: 0.98.**

12. **Kotomin**, **E**.**A**., **Kuzovkov**, **V**.**N**., **Popov**, **A**.**I**., and Vila, R. Kinetics of *F* center annealing and colloid formation in Al_2O_3. - *Nuclear Instruments and Methods in Physics Research Section B: Beam Interactions with Materials and Atoms*, *374*, p. 107-110 (2016). **SNIP: 0.98.**

13. **Lisovski**, **O**., **Chesnokov**, **A**., **Piskunov**, **S**., **Bocharov**, **D**., **Zhukovskii**, **Y**u.**F**., Wessel, M., and Spohr, E. *Ab initio* calculations of doped TiO_2 anatase (101) nanotubes for photocatalytical water splitting applications. - *Materials Science in Semiconductor Processing*, *42*, 138-141 (2016). **SNIP: 0.94.**

14. **Piskunov**, **S**., Žguns, P.A., **Bocharov**, **D**., Kuzmin, A., Purans, J., Kalinko, A., Evarestov, R.A., Ali, S.E., and Rocca, F. Interpretation of unexpected behavior of infrared absorption spectra of ScF_3 beyond the quasiharmonic approximation. - *Physical Review B, 93*(21), 214101 (2016). **SNIP: 0.94.**

15. Karbovnyk, I., Olenych, I., Kukhta, A., Lugovskii, A., Sasnouski, G., Olenych, Y., Luchechko, A., **Popov, A.I.**, and Yarytska, L.. Multicolor photon emission from organic thin films on different substrates. - *Radiation Measurements*, *90*, p. 38-42 (2016)**. SNIP: 0.86.**

16. Klym, H., Ingram, A., Shpotyuk, O., Hotra, O., and **Popov, A.I.** Positron trapping defects in free-volume investigation of Ge–Ga–S–CsCl glasses. - *Radiation Measurements*, *90*, p. 117-121 (2016). **SNIP: 0.86**.

17. **Mastrikov**, **Yu**.**A**., Guo, S., Puleo, F., Liotta, L. F., and **Kotomin**, **E**.**A**. First principles modeling of Pd-doped (La,Sr)(Co,Fe)O_3 complex perovskites. - *Fuel Cells*, *16*(2), p. 267-271 (2016). **SNIP: 0.77**.

18. **Zhukovskii**, **Yu**.**F**., **Piskunov**, **S**., **Lisovski**, **O**., Spohr, E., and Evarestov, R.A. Quantum chemical simulations of doped ZnO nanowires for photocatalytic hydrogen generation. - *physica status solidi (b)*, *253*(11), p. 2120-2128 (2016). **SNIP: 0.74**.

19. **Gopejenko**, **A**., **Zhukovskii**, **Yu**.**F**., **Kotomin**, **E**.**A**., **Mastrikov**, **Yu**.**A**., Vladimirov, P.V., Borodin, V.A., and Möslang, A. Ab initio modelling of Y–O cluster formation in γ-Fe lattice. - *physica status solidi (b)*, *253*(11), 2136-2143 (2016). **SNIP: 0.74**.

20. **Dumbrajs**, **O.**, Saito, T., and Tatematsu, Y. Start-up scenario of a high-power pulsed gyrotron for 300 GHz band collective Thomson scattering diagnostics in the large helical device. - *Physics of Plasmas*, *23*(2), 023106 (2016). **SNIP: 0.61**.

21. **Dumbrajs**, **O**. and Nusinovich, G. S. Self-consistent non-stationary theory of the gyrotron. - *Physics of Plasmas*, *23*(8), 083125 (2016). **SNIP: 0.61**.

22. **Dumbrajs**, **O**., Saito, T., Tatematsu, Y., and Yamaguchi, Y. Influence of the electron velocity spread and the beam width on the efficiency and mode competition in the high-power pulsed gyrotron for 300 GHz band collective Thomson scattering diagnostics in the large helical device. - *Physics of Plasmas*, *23*(9), 093109 (2016). **SNIP: 0.61.**

23. Klym, H., Karbovnyk, I., Guidi, M.C., Hotra, O., and **Popov, A.I.** Optical and vibrational spectra of CsCl-Enriched GeS_2-Ga_2S_3 Glasses. - *Nanoscale Research Letters*, *11*(1), 132 (1-6) (2016). **SNIP: 0.61.**

24. **Popov, A.I.**, Lushchik, A., and **Kotomin, E.A.** Low-temperature radiation effects in wide gap materials. - *Low Temperature Physics*, *42*(7), p. 537-538 (2016). **SNIP: 0.60.**.

25. Kuzmin, A., Pankratov, V., Kalinko, A., Kotlov, A., Shirmane, L., and **Popov, A.I.**. UV-VUV synchrotron radiation spectroscopy of $NiWO_4$. - *Low Temperature Physics*, *42*(7), p. 543 (2016). **SNIP: 0.60**.

26. **Bocharov, D.**, Žguns, P., Piskunov, S., Kuzmin, A., and Purans, J.. Electronic structure of cubic ScF_3 from first-principles calculations. - *Low Temperature Physics*, *42*(7), p. 556 (2016). **SNIP: 0.60.**

27. **Klotins, E.** (2016). A novel quantum field approach to photoexcited insulators. - *Low Temperature Physics*, *42*(7), p. 570 (2016). **SNIP: 0.60**.

28. Mironova-Ulmane, N., Skvortsova, V., and **Popov, A.I.** Optical absorption and luminescence studies of fast neutron-irradiated complex oxides for jewellery applications. - *Low Temperature Physics*, *42*(7), p. 584 (2016). **SNIP: 0.60**.

29. **Kuzovkov, V.N.**, **Popov, A.I.**, **Kotomin, E.A.**, **Moskina, A.M.**, Vasil'chenko, E., and Lushchik, A. Theoretical analysis of the kinetics of low-temperature defect recombination in alkali halide crystals. - *Low Temperature Physics*, *42*(7), p. 588 (2016). **SNIP: 0.60**.

30. Karbovnyk, I., Bolesta, I., Rovetskyi, I., Lesivtsiv, V., Shmygelsky, Y., Velgosh, S., and **Popov**, **A.I.**. Long-term evolution of luminescent properties in CdI_2 crystals. - *Low Temperature Physics*, *42*(7), p. 594 (2016). **SNIP: 0.60**.

31. Savchyn, V.P., **Popov, A.I.**, Aksimentyeva, O.I., Klym, H., Horbenko, Y.Y., Serga, V., **Moskina, A.M.**, Karbovnyk, I. Cathodoluminescence characterization of polystyrene–$BaZrO_3$ hybrid composites. - *Low Temperature Physics*, *42*(7), p. 597 (2016). **SNIP: 0.60**.

32. Klym, H., Ingram, A., Shpotyuk, O., Hadzaman, I., Solntsev, V., Hotra, O., and **Popov, A.I.** Positron annihilation characterization of free volume in micro-and macro-modified $Cu_{0.4}Co_{0.4}Ni_{0.4}Mn_{1.8}O_4$ ceramics. - *Low Temperature Physics*, *42*(7), p. 601 (2016). **SNIP: 0.60**.

33. **Eglitis**, **R.I.**, **Piskunov**, **S.**, and **Zhukovskii**, **Yu.F.** *Ab initio* calculations of $PbTiO_3$/$SrTiO_3$ (001) heterostructures. - *physica status solidi (c)*, *13*(10-12), p. 913-920 (2016). **SNIP: 0.54**.

34. **Platonenko, A.**, **Gryaznov, D.**, **Piskunov, S.**, **Zhukovskii, Yu.F.**, and **Kotomin, E.A.** Charged oxygen interstitials in corundum: first principles simulations. - *physica status solidi (c)*, *13*(10-12), p. 932-936 (2016). **SNIP: 0.54**.

35. **Bocharov**, **D.**, Krack, M., Kalinko, A., Purans, J., Rocca, F., Ali, S.E., and Kuzmin, A. *Ab initio* molecular dynamics simulations of the Sc *K*-edge EXAFS of scandium trifluoride. - *Journal of Physics: Conference Series, 712*, 012009 (2016). **SNIP: 0.25**.

36. Purans, J., **Piskunov**, **S.**, **Bocharov**, **D.**, Kalinko, A., Kuzmin, A., Ali, S.E., and Rocca, F. Local structure of perovskites ReO_3 and ScF_3 with negative thermal expansion: interpretation beyond the quasiharmonic approximation. - *Journal of Physics: Conference Series, 712*, 012013 (2016). **SNIP: 0.25**.

37. **Bocharov**, **D.**, Chollet, M., Krack, M., Bertsch, J., Grolimund, D., Martin, M., Kmin, A., Purans, J. and **Kotomin, E.A.** Interpretation of the U L_3-edge EXAFS in uranium dioxide using molecular dynamics and density functional theory simulations. - *Journal of Physics: Conference Series*, *712*, 012091 (2016). **SNIP: 0.25**.

38. **Eglitis**, **R.I**. and **Piskunov**, **S**. First principles calculations of $SrZrO_3$ bulk and ZrO_2-terminated (001) surface *F* centers. - *Computational Condensed Matter*, *7*, p. 1-6 (2016). **SNIP: 0.21**.

Chapters in Scientific Books

1. M. Arrigoni, **E.A. Kotomin**, and J. Maier, Large scale modeling of defects in advanced oxides: Oxygen vacancies in $BaZrO_3$ crystals. - Chapter in a book: W. Nagel *et al.* (eds.) High Performance Computing in Science and Engineering, (Springer, Switzerland), 2016, p. 187-198.

2. **Yu.F. Zhukovskii**, **S. Piskunov**, **O. Lisovski**, **A. Chesnokov**, and **D. Bocharov**, First principle evaluation of photocatalytic suitability for TiO_2-based nanotubes. - Chapter in a book: W. Cao (Ed.) Semiconductor Photocatalysis - Materials, Mechanisms and Applications (InTech Open Access Publishers, Croatia), 2016, p. 105-133.

Non-SCI Publication

1. **Shunin**, **Yu**.**N**., Fink, D., Kiv, A.E., Alfonta, L., Mansharipova, A. , Muhamediyev, R., **Zhukovskii**, **Yu**.**F**., Lobanova-Shunina, T., Burlutskaya, N., Gopeyenko, V.I., and Bellucci, S.Theory and modelling of real-time physical and bio- nanosensor systems. - *Computer Modelling & New Technologies*, *20*(4), p. 7-17 (2016).

Presentations at Scientific Conferences, Meetings, and Workshops in 2016

I. Workshop on Fundamental Physics of Ferroelectrics (Washington, USA, January - February, 2016).

*1. M.M. Kuklja, **E.A. Kotomin**, D. Fuks, **Yu.A. Mastrikov**, and J. Maier, "Structural (in)stability of complex perovskites for solid oxide fuel cells: first principles calculations". Abstract, p. 25.*

*2. **E.A. Kotomin**, **Yu.A. Mastrikov**, R. Merkle, M.M. Kuklja, and J. Maier, "First principles calculations of oxygen vacancies in the bulk and on the surface of complex perovskites for solid oxide fuel cell cathodes". Abstracts, p.102.*

II. 32th ISSP Conference (Riga, Latvia, February, 2016).

*3. **A. Gopejenko**, **Yu.F. Zhukovskii**, P.V. Vladimirov, E.A. Kotomin, **Yu.A. Mastrikov**, V.A. Borodin, and A. Möslang, "Ab initio calculations of O and V_{Fe} interaction in fcc Fe lattice". Abstract: p. 37.*

*4. V. Savchyn, O. Aksimentyeva, H. Klym, I. Karbovnyk, E. Elsts, J. Jansons, and **A.I. Popov**, "Comparative studies of cathodoluminscence properties of acceptor-doped $BaZrO_3$ and $SrTiO_3$". Abstract: p. 52.*

*5. **O. Dumbrajs**, "Present status of design, development and validation of the European gyrotron for ITER". Abstract: p. 70.*

*6. I. Jonane, J. Timoshenko, A. Kuzmin, **D. Bocharov**, and M. Krack "Temperature dependence of the local structure of scandium fluoride". Abstract: p. 76.*

*7. **D. Bocharov**, M. Krack, A. Kuzmin, J. Purans, and A. Kalinko, "Study of negative-thermal expansion in ScF_3 using first principles ab initio molecular dynamics". Abstract: p. 92.*

*8. **A. Chesnokov**, **D. Grjaznov**, M. Arrigoni, and R.A. Evarestov. "Calculation of pure and doped cerium dioxide properties in bulk phase". Abstract: p. 93.*

*9. **A. Platonenko**, **Yu.F. Zhukovskii**, **S. Piskunov**, and **E.A. Kotomin**, "First principles calculations of interstitial oxygen atom migration paths in corundum". Abstract: p. 94.*

10. ***A. Gopejenko, Yu.F. Zhukovskii, S. Piskunov, E.A. Kotomin****, "Variation of Zr and Ti concentration in PZT: first principles calculations on the electronic structure". Abstract: p. 95.*

11. ***M. Sokolov, Yu.A. Mastrikov, A. Gopejenko, Yu.F. Zhukovskii****, and* ***E.A. Kotomin****,"Ab initio modelling of Y-O complexes in α-Fe matrix". Abstract: p. 97.*

III. 50th Russian School on Condensed State Physics (St. Petersburg, Russia, March, 2016).

12. ***D. Bocharov****, M. Krack, A. Kuzmin, and J. Purans, "Interpretation of EXAFS spectra using molecular dynamics: comparison of classical and ab initio approach". Abstract: p. 213.*

13. ***D. Bocharov****,* ***Yu.F. Zhukovskii****,* ***S. Piskunov****,* ***O. Lisovski****, and* ***A. Chesnoko****v, "First principles evaluation of photocatalytic suitability for TiO2-based nanotubes". Abstract: p. 214.*

IV. 14th International Conference "Information Technologies and Management", IT&M'2016 (Riga, Latvia, April, 2016).

14. ***Yu.N. Shunin****, L. Alfonta, D. Fink, A.E. Kiv, A. Mansharipova, R. Muhamediyev,* ***Yu.F. Zhukovskii****, and T. Lobanova-Shunina, "Modelling and simulation of electric response of nanocarbon nanocomposites and nanoporous polymer based structures for nanosensor devices". Abstract: p. 11-14.*

15. ***M. Sokolov****,* ***Yu.A. Mastrikov****,* ***A. Gopejenko****,* ***Yu.F. Zhukovskii****, and* ***E.A. Kotomin****, "Ab initio modelling of Y-O complexes in α-Fe matrix". Abstract: p. 18-19.*

16. ***Yu.F. Zhukovskii, O. Lisovski, S. Piskunov****, and R.A. Evarestov, "Suitability of doped [0001]-oriented ZnO nanowires of different sizes for photocatalytic applications: DFT-LCAO simulations". Abstract: p. 20-21.*

17. ***A. Gopejenko****,* ***Yu.F. Zhukovskii****,* ***S. Piskunov****, and* ***E.A. Kotomin****, "First principle calculations of PZT varying Zr and Ti concentrations". Abstract: p. 22.*

18. ***A. Platonenko****,* ***Yu.F. Zhukovskii****,* ***S. Piskunov****, and* ***E.A. Kotomin****, "Ab initio calculations of charged point defects in corundum". Abstract: p. 23.*

V. E-MRS 2016 Spring Meeting (Lille, France, May, 2016).

19. ***R.I. Eglitis****, "Comparative ab initio calculations of $SrTiO_3$, $BaTiO_3$, $PbTiO_3$ and $CaTiO_3$ (001), (011) as well as (111) surfaces". – Abstract: AA.P2.3.*

20. M. Arrigoni, ***E.A. Kotomin****, J. Maier,* ***D. Gryaznov****, and R.A. Evarestov, A comparative ab initio analysis of oxygen vacancies on CeO_2(111) surfaces and in the bulk". - Abstract: BB.1.3.*

21. H. Klym, A. Ingram, I. Karbovnyk, O. Shpotyuk, and ***A.I. Popov****, "Influence of water-sorption processes on free-volume defects near grain boundaries in nanostructured MgO-Al_2O_3 ceramics". – Abstract: BB.1.6.*

22. ***A.I. Popov****,* ***E.A. Kotomin****,* ***V.N. Kuzovkov****, A. Lushchik, V.M. Lisitsyn, A. Akilbekov, and J. Maier, "Modelling of F center annealing kinetics in neutron- and electron-irradiated MgF_2 and MgO crystals". – Abstract: BB.8.2.*

23. ***R.I. Eglitis****,* ***S. Piskunov****, and* ***Yu.F. Zhukovskii****, "Ab initio calculations of $SrZrO_3$ bulk and surface F centers as well as $BaTiO_3$/$SrTiO_3$, $SrZrO_3$/$PbZrO_3$, and $SrTiO_3$/$PbTiO_3$ heterostructures". – Abstract: BB.8.3.*

*24. **Yu.A. Mastrikov**, P.V. Vladimirov, V.A. Borodin, **A. Gopejenko**, **Yu.F. Zhukovskii**, **E.A. Kotomin**, and A. Möslang,"Ab initio modelling of nY/mO nanoclusters in bcc Fe lattice". – Abstract: BB.9.2.*

*25. **Yu.F. Zhukovskii**, **O. Lisovski**, **S. Piskunov**, and R.A. Evarestov, "Quantum chemical simulations of doped ZnO nanowires for photocatalytic hydrogen generation". – Abstract: BB.13.2.*

*26. **A.I. Popov**, **E.A. Kotomin**, **V.N. Kuzovkov**, A. Lushchik, E. Shablonin, and E. Vasil'chenko, "Comparison of the diffusion-controlled F center thermal annealing in neutron- and heavy-ion irradiated Al_2O_3 crystals". – Abstract: BB.P1.6.*

*27. **A. Platonenko**, **Yu.F. Zhukovskii**, **S. Piskunov**, and **E.A. Kotomin**, "Ab initio simulations of radiation-induced oxygen defects in corundum". – Abstract: BB.P1.8.*

*28. **Yu.A. Mastrikov**, R. Merkle, **E.A. Kotomin**, M.M. Kuklja, and J. Maier, "Effect of (La,Sr)MnO3 (001) surface terminations on oxygen reduction reaction rate". – Abstract: D.1.3.*

*29. **D. Gryaznov**, R. Merkle, **E. A. Kotomin**, and J. Maier, "First principles calculations of protonic defects in $La_{1-x}Sr_xFeO_3$-delta perovskites". – Abstract: D.3.3.*

*30. **E.A. Kotomin**, M. Arrigoni, J. Maier, and T.S. Bjørheim, "Confinement effects for oxygen vacancies in $BaZrO_3$ ultrathin films". – Abstract: D.13.7.*

*31. I. Karbovnyk, I. Olenych, O. Aksimentyeva, A. Stelmashchuk, and **A.I. Popov**, "Nanotubes and nanoparticles in polymer matrices: effect of radiation on physical properties". – Abstract: J.P28.*

*32. **A.I. Popov**, O.I. Aksimentyeva, H. Klym, I. Karbovnyk, E. Elsts, and V.P. Savchyn, "Cathodoluminescence study of acceptor-doped $BaZrO_3$ and $SrTiO_3$". – Abstract: L.P40.*

*33. **R.I. Eglitis**, "Theoretical prediction of the 5 Volt rechargeable Li ion battery using $Li_2CoMn_3O_8$ as a cathode". – Abstract: U.P1.18.*

VI. School-conference on "Atomistic Simulations of Functional Materials" (Moscow, Russia, May, 2016).

*34. **E.A. Kotomin**, "Ab initio calculations of defects in perovskite crystals for fuel cell applications".*

VII. Functional Oxide Surfaces and Interfaces (FOXSI), (Vienna, Austria, May, 2016).

*35. **D. Gryaznov**, R. Merkle, **Yu.A. Mastrikov**, **E.A. Kotomin**, and J. Maier, "Mechanism of the oxygen reduction reaction at SOFC cathodes: combined experimental and ab-initio investigations".*

VIII. 6th International Colloids Conference (Berlin, Germany, June, 2016).

*36. **V.N. Kuzovkov**, **E.A. Kotomin**, A. Lushchik, and **A.I. Popov**, "Diffusion-controlled kinetics of metallic colloid formation in ionic crystals". Abstract: P006.*

*37. **V.N. Kuzovkov**, G. Zvejnieks, **E.A. Kotomin**, and P. Merzlyakov, "Modelling of metal colloid superlattice formation inirradiated wide gap insulators". Abstract: P007.*

IX. 12th International Conference on Diffusion in Solids and Liquids, DSL 2016 (Split, Croatia, June, 2016).

*38. **V.N. Kuzovkov**, **E.A. Kotomin**, A. Lushchik, and **A.I. Popov**, "The kinetics of diffusion-controlled recombination of radiation-induced defects in ionic solids". Abstract: DSL122.*

X. 12th International Symposium on Systems with Fast Ionic Transport, ISSFIT-12 (Kaunas, Lithuania, July, 2016).

39. ***E.A. Kotomin****,* ***Yu.A. Mastrikov****, and J. Maier, "Structural stability of complex perovskites for solid oxide fuel cells: first principles thermodynamic calculations". Abstracts: p. 15.*

40. ***A.I. Popov****,* ***E.A. Kotomin****, and J.Maier, "Analysis of the self-trapped hole mobility and recombination in alkali halides and complex metal oxides". Abstracts: p. 115.*

XI. College on Multiscale Computational Modeling of Materials for Energy Applications (Trieste, Italy, July 2016).

41. ***O. Lisovski****,* ***S. Piskunov****,* ***Yu.F. Zhukovskii****, and E. Spohr, "DFT modeling of doped ZnO nanowires with various diameters".*

XII. The 19th International Conference on Defects in Insulating Materials, ICDIM'16 (Lyon, France, July, 2016).

42. R.A. Evarestov , ***Yu.F. Zhukovskii****,* ***S. Piskunov****,* ***A. Platonenko****,* ***E.A. Kotomin****, and J. Maier, "Ab initio simulations of interstitial oxygen in corundum". Abstract: Mo-O-15.*

XIII. 5th International Workshop on Nanocarbon Photonics and Optoelectronics (Lappeenranta, Finland, August, 2016).

43. ***Yu.N. Shunin****, D. Fink, A.E. Kiv, L. Alfonta, A. Mansharipova, R. Muhamediyev,* ***Yu.F. Zhukovskii****, T. Lobanova-Shunina, N. Burlutskaya, V.I. Gopeyenko, and S. Bellucci, "Theory and modelling of physical and bio- nanosensor systems". Abstract: p. 101.*

XIX. 29th Symposium On Fusion Technology (Prague, Czech republic, September, 2016).

44. ***A.I. Popov****,* ***E.A. Kotomin****,* ***V.N. Kuzovkov****, A. Lushchik, and R. Vila, Diffusion-controlled F center thermal annealing in neutron, electron and heavy-ion irradiated insulators". Abstracts: P3.184*

XX. E-MRS 2016 Fall Meeting (Warsaw, Poland, September, 2016).

45. ***A. Platonenko****,* ***D. Bocharov****,* ***S. Piskunov****,* ***Yu.F. Zhukovskii****, E. Spohr, and P.N. D'yachkov, "Computer modeling of 3d-metal doped fluorite-structured TiO_2 (4,4) nanotubes for efficient hydrogen synthesis from water". Abstract: D.11.2.*

46. ***A. Platonenko****,* ***D. Gryaznov****,* ***Yu.F. Zhukovskii****,* ***S. Piskunov****, and* ***E.A. Kotomin****, "Ab initio simulations on migration paths of charged oxygen interstitials in corundum". Abstract: T.P.5.*

47. ***D. Bocharov****, M. Krack, A. Kuzmin, and J. Purans, "Calculations on structural properties of pure and chromium doped uranium dioxide". Abstract: T.P.9.*

48. ***D. Bocharov****, Yu. Rafalskij, M. Krack, A. Kalinko, S.E. Ali, F. Rocca, R.A. Evarestov, A. Kuzmin, and J. Purans, "Ab initio molecular dynamics study of negative thermal expansion in ScF_3". Abstract: U.11.1.*

XXI. IRMMW-THz 2016 conference (Copenhagen, Denmark, September, 2016).

49. ***O. Dumbrajs****, T. Saito, Y. Tatematsu, and Y. Yamaguchi, "Start-up scenario of a high-power pulsed gyrotron for 300 GHz band collective Thomson scattering diagnostics in the Large Helical Device".*

XXII. EU-Japan-USA RF Heating Technology Workshop (Leinsweiler, Germany, September, 2016).

50. ***O. Dumbrajs*** *and G.S. Nusinovich, "Self-consistent non-stationary theory of gyrotrons".*

XXIII. 25th IEA Annex II Workshop on Radiation Effects in Ceramic Insulators Satellite Meeting during SOFT-29 (Prague, Czech Republic, September, 2016).

51. ***A.I. Popov****, "Thermal annealing of point defects in irradiated insulators".*

XXIV. 18th International Conference on Solid State Protonic Conductors (SSPC-18), (Oslo, Norway, September, 2016).

52. ***D. Gryaznov****, R. Merkle,* ***E.A. Kotomin****, and J. Maier, "First-principles calculations of protonic defects in (La,Sr)FeO_3 perovskites." - Abstract: p.166.*

XV. 17th International Workshop on Nanoscience and Nanotechnology, n&n-2016 (Frascati, Italy, September, 2016).

53. ***Yu.N. Shunin****, D. Fink, A.E. Kiv, L. Alfonta, A. Mansharipova, R. Muhamediyev,* ***Yu.F. Zhukovskii****, T. Lobanova-Shunina, N. Burlutskaya, V.I. Gopeyenko, and S. Bellucci, "Physical and bio- nanosensors for medical applications and ecological monitoring". Abstract: p. 50-52.*

XVI. International school on Electrochemical Energy Conversion and Storage (Stuttgart, Germany, October, 2016).

54. ***E.A. Kotomin****, "Ab initio calculations for oxide functional materials".*

XVII. The Nuclear Materials Conference, (Montpellier, France, November, 2016).

55. ***A.I. Popov****,* ***Yu.F. Zhukovskii****,* ***E.A. Kotomin****,* ***A. Platonenko****,* ***S. Piskunov****,* ***V.N. Kuzovkov****, A. Lushchik, and R. Vila, "Computer simulations of radiation damage and defect recombination kinetics in sapphire". Abstract: P.1.72.*

==========